

2 (199-



This is to certify that the

thesis entitled

TEXTURE ANALYSIS OF GAMMA-BASED TITANIUM
ALUMINIDE IN COMPRESSION
AT ROOM TEMPERATURE AND ELEVATED TEMPERATURES

presented by

Soonwuk Cheong

has been accepted towards fulfillment of the requirements for

Master's degree in Materials Science

Major professor

Date 12 December 1995

MSU is an Affirmative Action/Equal Opportunity Institution

**O**-7639

# LIBRARY Michigan State University

PLACE IN RETURN BOX to remove this checkout from your record. TO AVOID FINES return on or before date due.

DATE DUE	DATE DUE	DATE DUE
- (1) mg - 1		
723 0.2 1998 2000 0 9 1078		
, p. 3 - 1		
Wind & west		

MSU is An Affirmative Action/Equal Opportunity Institution

## TEXTURE ANALYSIS OF GAMMA-BASED TITANIUM ALUMINIDE IN COMPRESSION AT ROOM TEMPERATURE AND ELEVATED TEMPERATURES

By

Soonwuk Cheong

#### **A THESIS**

Submitted to

Michigan State University

in partial fulfillment of the requirements

for the degree of

MASTER OF SCIENCE

**Department of Materials Science and Mechanics** 

1995

#### **ABSTRACT**

## TEXTURE ANANLYSIS OF GAMMA-BASED TITIANIUM ALUMINIDE IN COMPRESSION

#### AT ROOM TEMPERATURE AND ELEVATED TEMPERATURES

By

#### Soonwuk Cheong

Deformation of TiAl based materials is affected by the way strain is distributed between three distinct deformation systems, 1/2<110] normal dislocation slip on the basal plane, <011] super-dislocation slip out of the basal plane, and mechanical twinning resulting from 1/6<112] dislocation motion. Prior work has shown that the relative contributions of these three deformation systems affects the amount of strain that occurs before fracture. Since mechanical twinning results in a dramatic change in crystal orientation, changes in texture after 5-10% strain were investigated on the surface of compression specimens deformed at 22, 650 and 850°C. With these small strains, changes in crystal orientation due to dislocation slip are small, on the order of a few degrees. Large changes in orientation observed in texture measurements were shown to be consistent with crystal rotations resulting from twinning. Estimations of the volume fraction of twinned crystals were obtained, and the maximum contribution of mechanical twinning to deformation occurred at 650°C, where mechanical twinning accounted for as much as 50% of the total strain.

## **TABLE OF CONTENTS**

LIST OF FIGURESv
LIST OF TABELS ix
1. INTRODUCTION
2. LITERATURE SURVEY
2.1 THE MICROSTRUCTURE
2.1.1 Crystal Structure
2.1.2 Phase Diagram
2.1.3 Microstructure
2.2 MECHANICAL BEHAVIOR
2.2.1 Effects of lamellar grains
2.2.2 Temperature Effect
2.2.3 Strain Rate
2.2.4 Yield Stress Behavior on DBTT
2.3 TWINNING AND SLIP IN TIAL
2.3.1Deformation Twinning
2.3.2 Twinning in TiAl
2.3.3 Plasticity of TiAl
2.4 DESCRIPTION OF TEXTURE
2.4.1 Definition of Texture
2.4.2 Eulerian Angles
2.4.3 Eulerian Angles and Miller Indices
2.4.4 Pole Figures and Inverse Pole Figures

2.5 PLASTIC DEFORMATION OF POLYCRYSTAL
2.5.1 Plastic Deformation in Polycrystal
2.5.2 Formation of Deformation Texture
2.5.3 The effect of Stacking Fault Energy on Deformation Texture 40
3. EXPERIMENTAL PROCEDURE
3.1 SPECIMEN PREPARATION
3.2 EXPERIMENTAL PROCEDURES FOR COMPRESSION TESTS 4
3.2.1 Compression test system
3.2.2 Compression test procedures
3.3 TEXTURE MEASUREMENT48
3.3.1 Texture measurement
3.3.2 Procedures in using popLA
<b>4. RESULTS</b>
4.1 STRESS-STRAIN BEHAVIOR
4.2 TEXTURE AFTER COMPRESSION
4.2.1 Texture at room temperature
4.2.2 Texture at 650°C and 850°C
5. ANALYSIS AND DISCUSSION
5.1 TEXTURE FORMATION
5.2 THE PREDICTION OF TWINNING
5.2.1 Schmid Law
5.2.2 Detection of Mechanical Twinning
5.2.3 Volume Fraction of Twinning

5.3 MAIN COMPONENT OF TEXTURE96	
5.4 MECHANISM OF TEXTURE FORMATION96	
5.4.1 Grain Rotation	
5.4.2 Slip	
5.4.3 Mechanical Twinning	
5.4.4 Dynamic Recrystallization	
5.4.5 Crack formation and deformation of TiAl99	
<b>6. CONCLUSION</b>	
7. REFERENCES	

.

## **FIGURES**

2.1 (a) Lattice structure of L1 <sub>o</sub> (b) Lattice structure of DO <sub>19</sub>
2.2 (a) A comparison of the Margolin and Murray Ti-Al phase diagram (b) The central portion of the recently refined TiAl phase diagram 6
2.3 The three types of lamellar structures 8
2.4 <110> directions and the atomic arrangement on a (111) plane in L1 $_0$ and <11 $\overline{2}$ 0> directions and the atomic arrangement on the basal plane in DO $_{19}$ 10
2.5 The stereographic projection of (111) $\gamma$ and (0001) $\alpha_2$ showing the six possible orientation variants of <110> $\gamma$ with respect to <1120> $\alpha_2$ matrix 11
2.6 The compositional effect on the room-temperature tensile properties of γ-base alloys at HIPed condition
2.7 Tensile test data if single phase TiAl (60 pct Ti-40 pct Al) from 25 to 1000°C with yield strength and fracture strength
2.8 The spatial relationships are given $K_1,K_2,\eta_1,\eta_2$ and the plane of shear $\ldots 21$
2.9 The atomic arrangement on the (111) plane
2.10 The atomic arrangement (a) true twinning (b) pseudo twinning
2.11 The sample fixed coordinate system K <sub>s</sub> and the crystal coordinate system K <sub>c</sub> in the sheet
2.12 The definition of the Euler angles
2.13 Orientation Distribution
2.14 The Euler space
2.15 Yield Locus and Latent Hardening
2.16 Lines of maximum descent from the point of maximum resolved shear stress  F and directions of rotation

<ul><li>2.17 (a) General trends of rotation in copper under tension</li><li>(b) General trends of rotation in α-brass under tension</li></ul>
2.18 (a) General trends of rotation in copper under compression (b) General trends of rotation in α-brass under compression
2.19 (a) Formation of Copper rolling orientation (b) Orientation paths due to mechanical twinning
3.1 The schematic view of compression test system
3.2 (a) Shape of specimen (b) Specimen orientation in the specimen holder
3.3 Comparison between compliance and compression curves at room temperature54
3.4 Comparison between compliance and compression curves at 650°C 55
3.5 Comparison between compliance and compression curves at 850oC 56
3.6 Stress-Strain Curves at three temperatures
4.1 (111) Pole Figures before and after compression at room temperature 62
4.2 (200) Pole Figures before and after compression at room temperature 63
4.3 (220) Pole Figures before and after compression at room temperature 64
4.4 (a) (111) Pole Figures before and after compression at 650°C
(b) (111) Pole Figures before and after compression at 850°C
<ul> <li>4.5 (a) (200) Pole Figures before and after compression at 650°C</li> <li>(b) (200) Pole Figures before and after compression at 850°C 66</li> </ul>
<ul> <li>4.6 (a) (220) Pole Figures before and after compression at 650°C</li> <li>(b) (220) Pole Figures before and after compression at 850°C 67</li> </ul>
5.1 Complete SODF after compression at room temperature in inside specimen 69
5.2 Complete SODF after compression at room temperature in outside specimen . 70
5.3 Complete SODF after compression at 650°C

5.4 Complete SODF after compression at 850°C
<ul><li>5.5 (a) Inverse pole figures before and after compression in inside specimen</li><li>(b) Inverse pole figures before and after compression in inside specimen 73</li></ul>
5.6 (a) Inverse pole figures before and after compression at 650°C  (b) Inverse pole figures before and after compression at 850°C
5.7 (a) Tension (b) Compression deformation geometry
5.8 Schmid factor contours with respect to the true twinning system of (111)[112] for tension and compression
5.9 (111) Pole Figures before and after twinning
5.10 Several stress axis orientations in 001 101 111 unit triangle
5.11 (110) component density diagram before and after compression at room temperature
5.12 (110) component density diagram before and after compression at 650°C and 850°C85
5.13 (a) Substraction of textured region from initial orientation distribution (b) Substraction of initial orientation distribution from textured state for normal direction in inverse pole figure at room temperature
5.14 (a) Substraction of textured region from initial orientation distribution (b) Substraction of initial orientation distribution from textured state for normal direction in inverse pole figure at 650°C
5.15 (a) Substraction of textured region from initial orientation distribution (b) Substraction of initial orientation distribution from textured state for normal direction in inverse pole figure at 850°C
5.16 SOD sections which include twinning component after deformation at room temperature
5.17 SOD sections which include twinning component after deformation at 650°C
5.18 SOD sections which include twinning component after deformation at 850°C

## **TABLES**

3.1 Chemical composition of specimen	43
3.2 The order of experiments and conditions of each test	48
5.1 Schmid factors of several deformation systems according to stress axis orientations	83
5.2 Euler angles for twinned components	90
5.3 Data of strain due to mechanical twinning	94

#### 1. INTRODUCTION

There is at present a great deal of interest in the intermetallic compound TiAl. This material has attractive properties, such as a high melting temperature, a low density, a high modulus, and good oxidation resistance. But low room-temperature ductility and poor formability of this material prevent many industrial applications. The deformation behavior of TiAl is related to its L1<sub>0</sub> crystal structure, which is based on an ordered face centered tetragonal cell in which the Ti and Al atoms occupy alternating (002) planes. The slip phenomena which include the normal slip of 1/2<110] dislocations and the superdislocation slip of <011] type dislocations in {111} slip planes has only recently been explained. Twinning on {111} planes is also an important mode of deformation. These deformation modes lead to strongly anisotropic deformation behavior.

Many important materials, such as metals, ceramics and some plastics, are polycrystalline structures. When the properties of their constituent crystals are strongly directionally dependent, the crystallographic orientations of the crystallites within the polycrystalline aggregate play an important role in the properties of the material. Texture is a fundamental material parameter that describes the overall characteristics of polycrystal materials in a macroscopic view.

The present work is concerned with studies of the deformation mechanisms of gamma-based TiAl alloys at room temperature and elevated temperatures. A major emphasis was to characterize the deformation behavior of polycrystalline TiAl through

texture analysis. In addition, the possibility to detect and quantify the formation of mechanical twins after compression was investigated. Since the  $L1_0$  crystal structure is similar to FCC metals, comparison of texture development on TiAl and FCC metals is useful to determine the important differences that are caused by the  $L1_0$  structure.

### 2. LITERATURE SURVEY

#### 2.1 THE MICROSTRUCTURE

#### 2.1.1 Crystal Structure

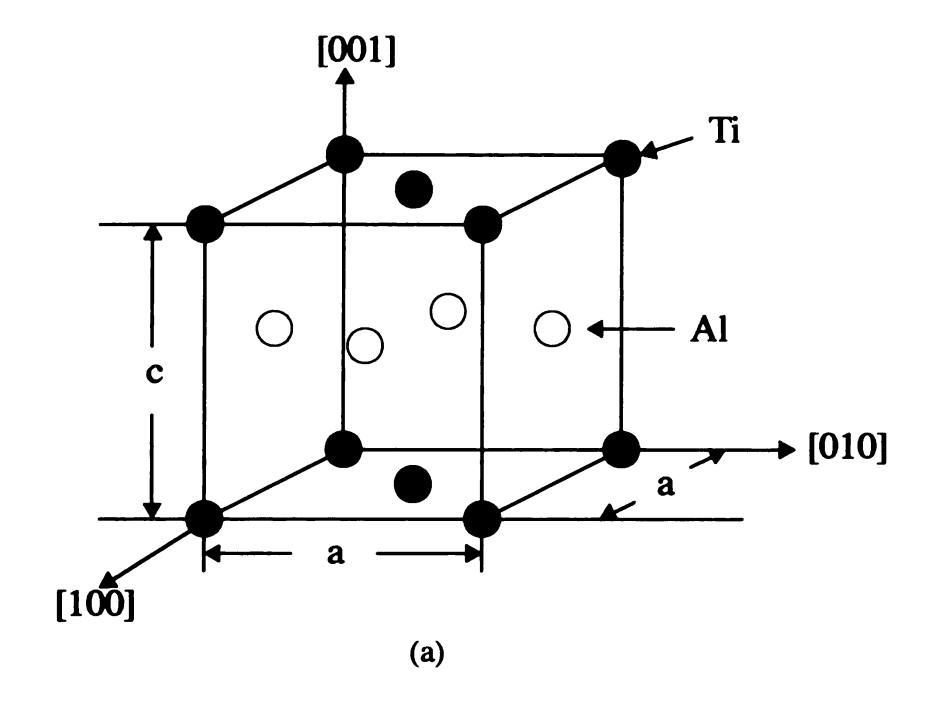
The  $\gamma$  phase of TiAl has the L1<sub>0</sub> crystal structure, which is based on an ordered face centered tetragonal cell in which the Ti and Al atoms occupy alternating (002) planes. This phase has a wide range of solubility (49-66 at.% aluminum) that varies with temperature. The tetragonality ranges from c/a ratios between 1.02 and 1.03 (Figure 2.1.(a)). The  $\alpha_2$  (DO<sub>19</sub>) structure is based on the composition A<sub>3</sub>B and it is one of the most typical superlattice structures derived from h.c.p. lattice. The sequence ...ababab... in Figure 2.1. (b) represents the DO<sub>19</sub> structure [1].

#### 2.1.2 Phase Diagram

The microstructure of gamma titanium aluminide is fundamentally dependent on the composition. The binary phase diagram of Ti-Al has been under dispute especially in the high temperature region near the Ti rich boundary of  $\gamma$ -TiAl. There are two versions of the binary phase diagram. The first one is the Hansen-Murray version [2]. According to this version,  $\alpha$ -Ti is unstable at high temperature above 1250 °C and  $\beta$ -phase is in equilibrium with  $\gamma$ -phase (L1<sub>0</sub>). Then the  $\beta$ -phase undergoes a solid-state transformation to form the ( $\alpha_2$ + $\gamma$ ). The other version is the Jaffe-Margolin version [3,4]. In this version, the high temperature region is  $\alpha$ -Ti, i.e. the disordered solid solution based on the hexagonal close

packed structure of Ti. Figure 2.2.(a) shows the comparison of the two phase-diagrams [5].

The common factor between these two phase diagrams is the  $\alpha_2(DO_{19}) + \gamma$  eutectoid structure in the range between 40 and 50 at.%Al at room temperature. However, they support different high temperature history and phases which can influence the microstructural evolution. To decode this ambiguity, there have been efforts by several workers [6,7]. Even though the precise location of the phase boundary still remains under investigation, the recent experimental data have shown that the phase in equilibrium with  $\gamma$ -TiAl which is the near  $\gamma$ -region above 1250°C is the hexagonal close packed solid solution based on the  $\alpha$ -Ti, rather than the body centered form of  $\beta$ -Ti [7]. The most recent phase diagram is shown in Figure 2.2.(b) [8]. It shows the peritectoid reaction (L+ $\alpha(\alpha$ -Ti)  $\rightarrow \gamma$ ) and the eutectoid reaction ( $\alpha \rightarrow \alpha_2 + \gamma$ ), which are different transformation history from the Hansen-Murray version.



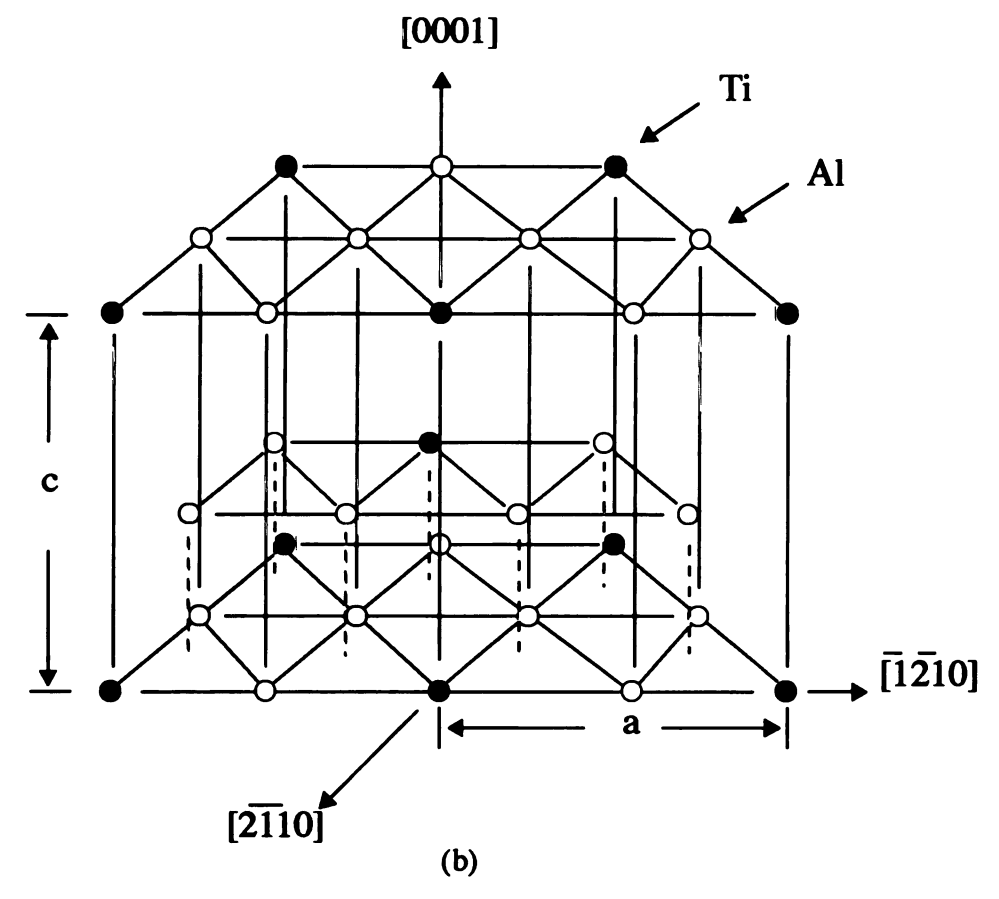


FIGURE 2.1. (a) Lattice structure of  $L1_0$  (b) Lattice structure of  $DO_{19}$  [1]

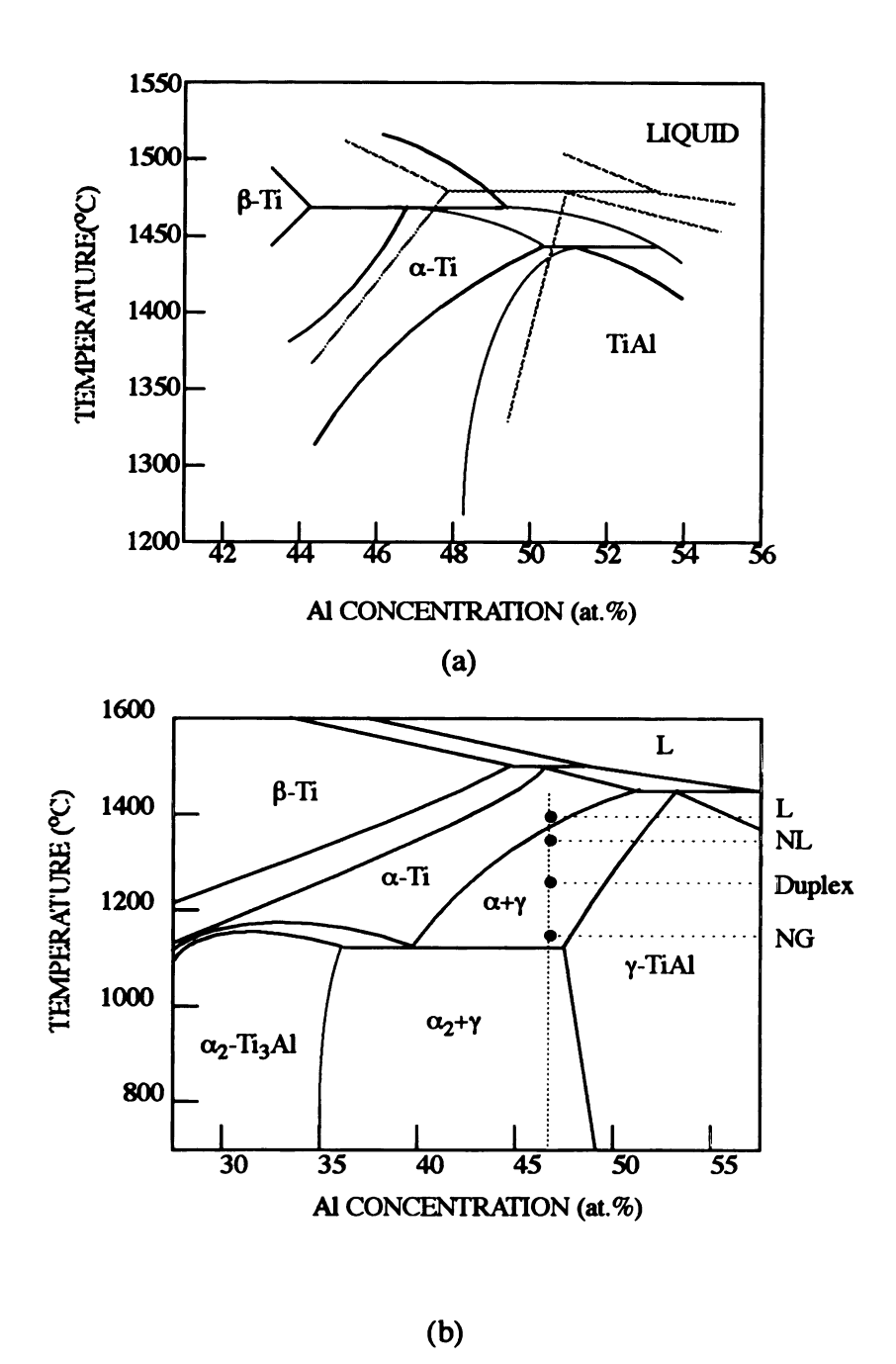


FIGURE 2.2. (a) A comparison of the Jaffe-Margolin (Solid lines) and Hansen-Murray (dashed lines) Ti-Al phase diagram. The Hansen-Murray diagram shows that  $\alpha$ -Ti does not exist above  $\sim 1285^{\circ}$ C [5]. (b) The central portion of the recently refined TiAl phase diagram and dashed lines indicate the microstructure changes according to heat treatment conditions (L: lamellar, NL: near lamellar, Duplex and NG: near gamma structures) [8].

#### 2.1.3 Microstructure.

The microstructure of TiAl varies largely according to the aluminum content. Generally, as-cast stoichiometric TiAl shows a microstructure consisting of grains of TiAl( $\gamma$ )-Ti<sub>3</sub>Al( $\alpha_2$ ) lamellar structure together with equiaxed  $\gamma$  grains. Aluminium rich single phase alloys are not of engineering importance because of their poor ductility and fracture toughness. The two phase microstructure, TiAl-Ti<sub>3</sub>Al, has more ductility than the single phase alloy, but the room temperature ductility is still limited to  $2\sim3\%$  [8,9]. The microstructure of TiAl is also sensitive to cooling rate, so it can vary from a duplex microstructure containing the  $\alpha_2/\gamma$  lamellar structure together with  $\gamma$  grains to a very fine lamellar structure with Widmannstatten-type morphology [10,11,12].

Since the existence of the two phase lamellar structure in the duplex structure has a considerable effect on mechanical properties, the following two factors are important in controlling the mechanical properties. The first one is the size of TiAl-Ti<sub>3</sub>Al two phase lamellar grains and TiAl single phase equiaxed grains. The second one is the volume fraction and distribution of lamellar grains. Therefore, understanding of the phase transformation is quite important because the final microstructure depends on the phase transformation history. The microstructure of gamma alloys may be classified into four groups: near-gamma, duplex, nearly lamellar and fully lamellar [13]. This classification is based upon heat treatment as illustrated in Figure 2.2(b). The NG (near -gamma) microstructures are obtained by a heat treatment just above the eutectoid temperature. The duplex microstructure is obtained after heat treatment at temperatures where equal amounts of  $\alpha$  and  $\gamma$  exist. The NL (nearly lamellar) microstructure is obtained at tempera-

tures where the predominant phase is alpha in the  $\alpha+\gamma$  region. The FL (fully lamellar) structure is obtained in the single phase  $\alpha$  field.

Three types of lamellar structures, called Types I, II and III, have been identified through several microstructural development studies [13,14,15]. The orientation relation between  $\alpha_2$  plates and gamma plates has been investigated through electron diffraction analysis and it shows that the phase transformation occurs during h.c.p.  $\rightarrow$  f.c.c. That is, the disordered h.c.p. phase that forms from the melt starts to order to the DO<sub>19</sub> structure at the h.c.p.  $\rightarrow$  f.c.c. transformation temperature (eutectoid temperature). Then, the DO<sub>19</sub>  $\rightarrow$  L1<sub>0</sub> phase transformation begins as the DO<sub>19</sub> phase cools down [16,17].

TYPE I: 
$$\alpha \longrightarrow \alpha + \gamma_p \longrightarrow L(\alpha/\gamma) \longrightarrow L(\alpha_2/\gamma)$$

TYPE II:  $\alpha \longrightarrow \alpha_2 \longrightarrow \alpha_2 + \gamma_{pt} \longrightarrow \alpha_2 + \gamma_p \longrightarrow L(\alpha_2/\gamma)$ 

TYPE III:  $\gamma_m + \alpha_2^p \xrightarrow{\text{heating}} \gamma_m + \alpha^p \longrightarrow \gamma_m + \alpha_p \longrightarrow L(\gamma/\alpha) \xrightarrow{\text{cooling}} L(\gamma/\alpha_2)$  (1)

$$\gamma_m \xrightarrow{\text{heating}} \gamma_m + \alpha_{pt} \longrightarrow \gamma_m + \alpha_p \longrightarrow L(\gamma/\alpha) \xrightarrow{\text{cooling}} L(\gamma/\alpha_2)$$
 (2)

FIGURE 2.3. The three types of lamellar structures [13]

The analysis indicates that the orientation relationship between  $\alpha_2$  and  $\gamma$  is  $\{0001\}\alpha_2$  //  $\{111\}\gamma$  and  $\{1120\}\alpha_2$  //  $\{110\}\gamma$ , which involves six possible orientation variants of  $\{110\}\gamma$  with respect to  $\{1120\}\alpha_2$  [18]. Figure 2.4 shows the orientation relationship between (111) plane which is the close-packed plane in TiAl and (0001) plane which is the basal plane in Ti<sub>3</sub>Al [1]. Figure 2.5 illustrates this relationships with the aid of the stereographic projection [19].

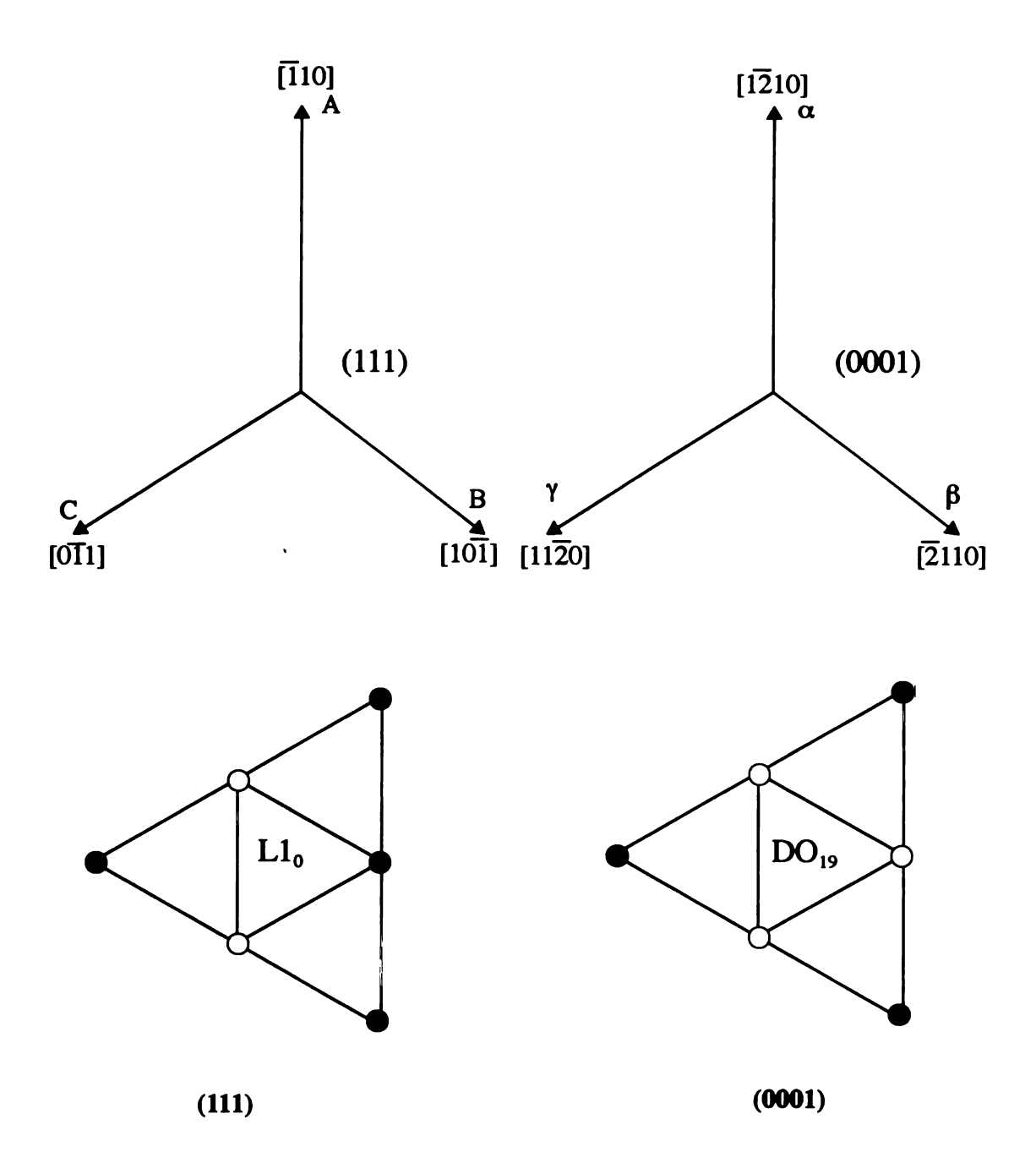


FIGURE 2.4. <110> directions and the atomic arrangement on a (111) plane in L1<sub>0</sub> and <11 $\overline{2}$ 0> directions and the atomic arrangement on the basal plane in DO<sub>19</sub> [1].

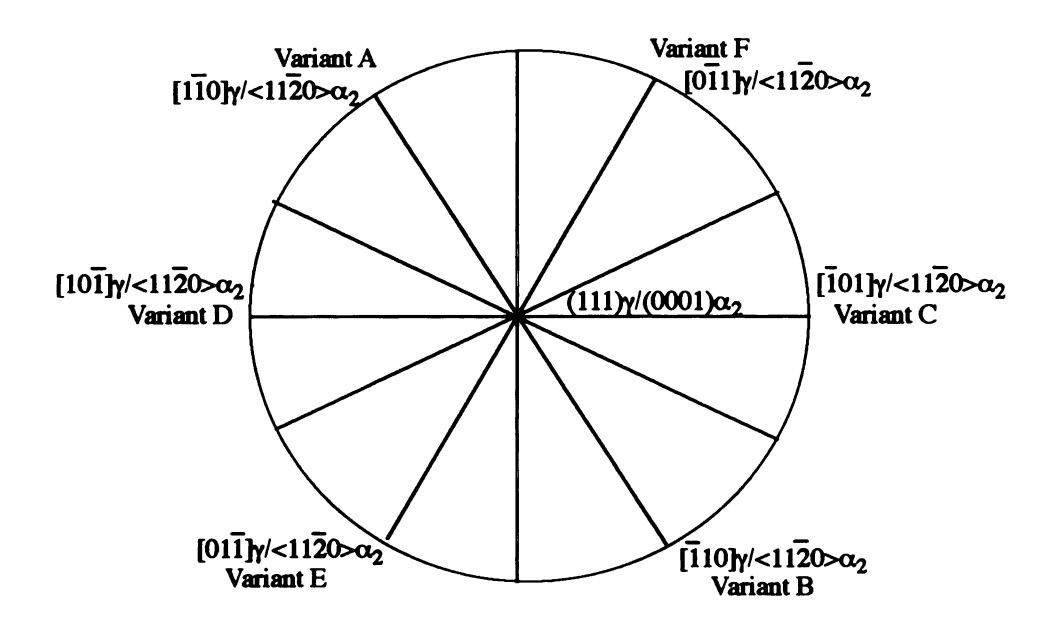


FIGURE 2.5. The stereographic projection of (111) $\gamma$  and (0001) $\alpha_2$  show the six possible orientation variants of <110> $\gamma$  with respect to <11 $\overline{2}$ 0> $\alpha_2$  matrix [19].

#### 2.2 MECHANICAL BEHAVIOR.

#### 2.2.1 Effects of lamellar grains

The ductility of gamma alloys is controlled by alloy chemistry and microstructure. Room temperature elongation of TiAl varies with aluminum content, exhibiting a maximum centered around the two-phase composition of Ti-48Al at HIPed (hot isostatic pressing) condition [20]. Figure 2.6 show the compositional effect on the room-temperature tensile properties of  $\gamma$ -base alloys [21]. Therefore, the strength of TiAl is thought to be related to the existence of  $\gamma$ - $\alpha_2$  lamellar grains [22,23]. The factors which can control the ductility in terms of microstructure distribution are:

- (i) the thickness of TiAl lamellae
- (ii) the size of ordered domains in TiAl lamellae
- (iii) the volume fraction, distribution, and thickness of Ti<sub>3</sub>Al lamellae
- (iv) the size of lamellar grains.

#### 2.2.2 Temperature Effect

In 1975, Lipsitt and colleagues presented the tensile test data for y - single phase alloy [24]. In their work, it was shown that the yield stress decreased with increasing deformation temperature, and that the yield stress dropped abruptly at the DBTT (Ductile-Brittle Transition Temperature) in the range 600°C to 900 °C. Recently, more intensive analysis of the yield behavior showed the relationship between the yield phenomena and the microstructure which is very sensitive to the Al content of TiAl [25,26,27]. Huang and Hall [25] and Rao and Tangri [26] noted the positive temperature dependence of the yield stress in high Al content alloy. Their results indicated that the yield stress dependence on temperature depends strongly on microstructure. Actually, they identified three different types of the yield behavior of TiAl, one for the single-phase  $\alpha_2$  alloy, one for the single phase y alloy and a third type for the two-phase alloy. For low Al content materials such as  $\alpha_2$  single phase, the yield stress decreased with increasing temperature. But for high Al content materials such as single phase  $\gamma$  alloy, the yield stress was irregular with increasing temperature, which indicates the influence of the positive temperature dependence of yield stress up to the DBTT. The two-phase alloys were insensitive to temperature. These differences in yield behavior can be explained by the different roles of the deformation mechanism in each phase. The content of Al of this alloy affects the final microstructure during heat treatment.

In the  $\gamma$  phase, there are 3 kinds of deformation possible, slip of normal 1/2 <110] dislocation, <101] superdislocation and twinning 1/6<11 $\overline{2}$ ]. The mixed general and specific brackets are normally used in TiAl, to recognize the anisotropic qualities of the L1<sub>0</sub> crystal structure (see Figure 2.1 (a)). The activity of each deformation system depends on the final microstructure. As temperature increases, the activity of each deformation mechanism changes due to thermal energy and this can affects their contribution to deformation [28]. Thus, the complexity of microstructure, deformation mechanism and thermal activation results in the different yield behaviors. But, this phenomena is most apparent below the DBTT. Above this range, decreasing yield stress with increasing temperature is a general situation for all three cases.

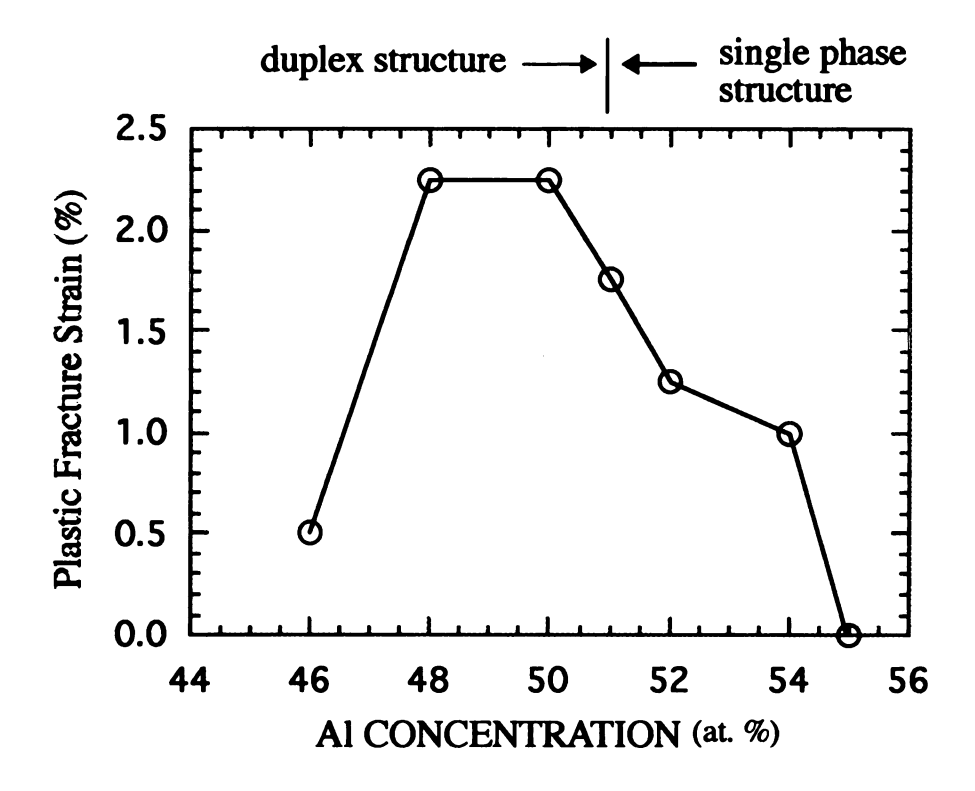


FIGURE 2.6. The compositional effect on the room-temperature tensile properties of  $\gamma$ -base alloys at HIPed condition [21].

#### STRENGTH OF TIAL AS A FUNCTION OF TEMPERATURE

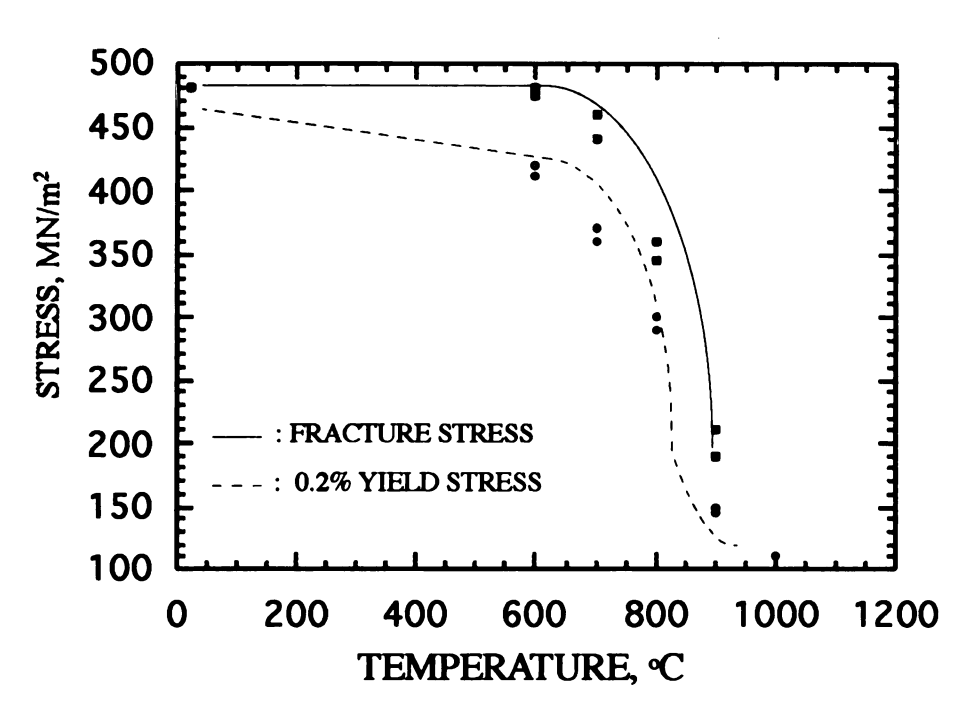


FIGURE 2.7. Tensile test data of single phase TiAl (60 pct Ti-40 pct Al) from 25 to 1000°C with yield strength and fracture strength [24].

#### 2.2.3 Strain Rate

Another factor which can influence the yield stress and elongation values is the strain rate [29]. While the mechanical behavior of titanium aluminides appears to be very sensitive to strain rate, limited work has been done. Shih and Schwartz recently found that a higher strain rate increases the DBTT [30]. Seetharman et al. showed a quantitative relationship between strain rate and DBTT enhancement [31]. But, the understanding of effects of strain rate on yield phenomena is still far from being complete.

#### 2.2.4 Yield Stress Behavior on DBTT (Ductile-Brittle Transition Temperature)

Recent experiments indicate that mechanical properties of this alloy also depend on both the area of grain boundaries and grain boundary structure which practically influences the interaction between lattice dislocations and grain boundaries [32,33,34]. The role of grain boundaries on mechanical behavior especially in the range of the DBTT was very important in the recent research by Imayev et al [33,34]. The brittleness of TiAl at room temperature results from the restrictions of normal slip caused by high Peierls stress and superdislocation slip by the anisotropic tetragonality of TiAl, which indicates that there is a low density of active sources of dislocations [25]. In addition, the shear transfer through the grain boundaries is difficult because of the blocking effect of grain boundaries at low temperature. These unfavorable conditions for plastic behavior of TiAl at low temperature localize the stress condition and initiate fracture instead of plastic deformation. However, as the testing temperature rises, deformation becomes delocalized. First, as temperature increases, the activation of each slip system increases, which results in increasing active

sources for plastic deformation. Secondly, the role of grain boundaries in deformation changes from an effective barrier for dislocation motion to a source or sink for dislocations. An increasing density of dislocations piled up at grain boundaries makes it easy to transfer the shear from one grain to another by building up low angle grain boundaries. Thus, The absorption of lattice dislocations in grain boundaries and the shear transfer from grain to grain increases the plasticity of TiAl in the ductile-brittle transition range.

#### 2.3 TWINNING AND SLIP IN TIAL.

#### 2.3.1 Deformation Twinning

The standard mode of twinning shown in Figure 2.8 is completely defined by the elements  $K_1$  and  $\eta_2$ , but it is common to use the four elements  $K_1$ ,  $K_2$ ,  $\eta_1$  and  $\eta_2$ .  $K_1$  is the twinning plane or the first undistorted plane in the twinning process;  $\eta_1$  is the direction of shear in the  $K_1$  plane.  $K_2$  is the second undistorted plane and  $\eta_2$  is the plane of shear [35]. The plane that lies perpendicular to  $K_1$  and contains the shear direction is called as the plane of shear. There are four twinning modes which fulfill the condition that the lattice is to be reproduced [36].

- (1) reflection in K<sub>1</sub>,
- (2) rotation of  $\pi$  about  $\eta_1$ ,
- (3) reflection in the plane normal to  $\eta_1$ ,
- (4) rotation of  $\pi$  about the normal to  $K_1$ .

In the first two modes,  $K_1$  and  $\eta_2$  are rational and in the last two modes,  $K_2$  and  $\eta_1$  are rational. When modes 1 and 2 occur simultaneously, the twinning is described as compound twinning, and this mode is observed in FCC crystals.

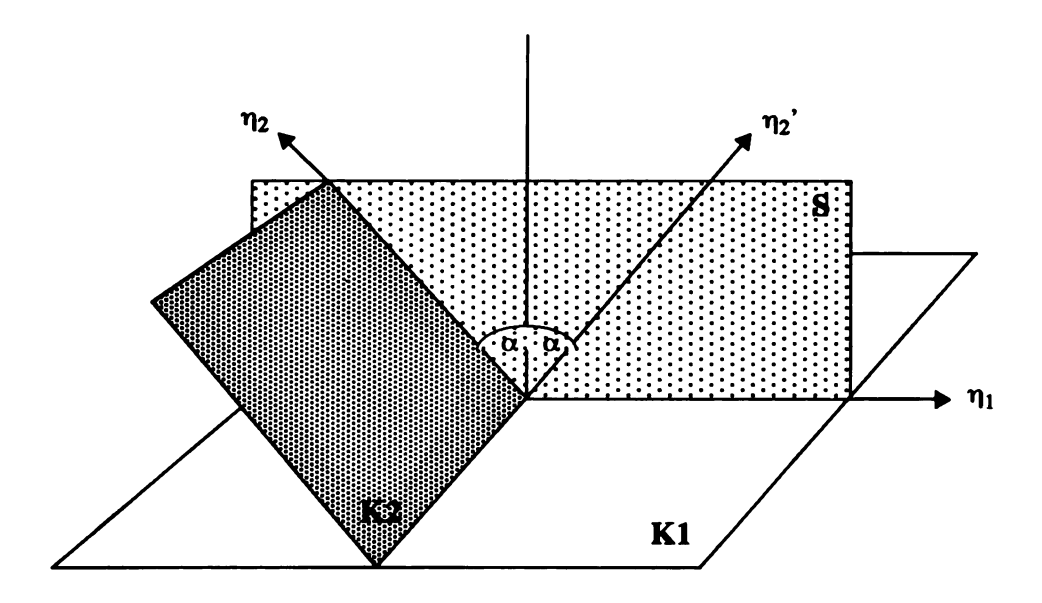
In FCC metals, the symmetry rule connecting the differently oriented parts is that one part is the mirror image of the other in a (111) plane. It can be observed that nearest neighbor relations are preserved at the boundary, but that an error in the stacking

sequences of the (111) planes occurs, such that the stacking sequence abcabc is turned into abcbac. For a shear of 0.707 the twinning elements are

$$K_1 = (111), \quad \eta_1 = [11\overline{2}], \quad K_2 = (11\overline{1}), \quad \eta_2 = [112]$$

#### 2.3.2 Twinning in TiAl.

In TiAl, there is a type of twin {111}<112> variant of the normal FCC twinning mode that causes an anti-phase boundary at the interface so that the twin plane is no longer a true reflecting plane. While the structure requirement for symmetry is met, the compositional symmetry is not, as illustrated in Figures 2.9 and 2.10. These are called pseudotwins, and 2 of the 3 possible twinning directions have this asymmetric nature where the L<sub>10</sub> structure is no longer preserved [37,38]. Figure 2.9 shows the stacking of (111) atomic planes in the sequence abcabc...[1,39,40]. When it is homogeneously sheared by operating one of the {111}[11\overline{2}> FCC true twinning systems, the symmetry of the L1<sub>o</sub> structure is preserved after twinning deformation. Since there is only one true twinning system in each {111} plane, and since twinning can only occur in one direction. There are only four true twinning systems,  $(111)[11\overline{2}]$ ,  $(1\overline{1}1)[1\overline{12}]$ ,  $(\overline{1}11)[\overline{1}1\overline{2}]$  and  $(\overline{11}1)[\overline{112}]$ . The number of operative twinning systems depends on the local grain orientation and principle stress state [41.42.43]. With a particular principle stress condition, only two true twinning systems which have components in the principle stress direction can possibly operate at one time.



### The summary of the basic nomenclature

 $K_1$ : the twinning plane, or the first undistorted plane

 $K_2$ : the second undistorted plane

 $\eta_1$ : the shear direction

 $\eta_2$ : the direction defined by the intersection of the plane of shear with  $K_2$ 

S: the plane of shear

FIGURE 2.8. The spatial relationships are given  $K_1$ ,  $K_2$ ,  $\eta_1$ ,  $\eta_2$  and the plane of shear [35].

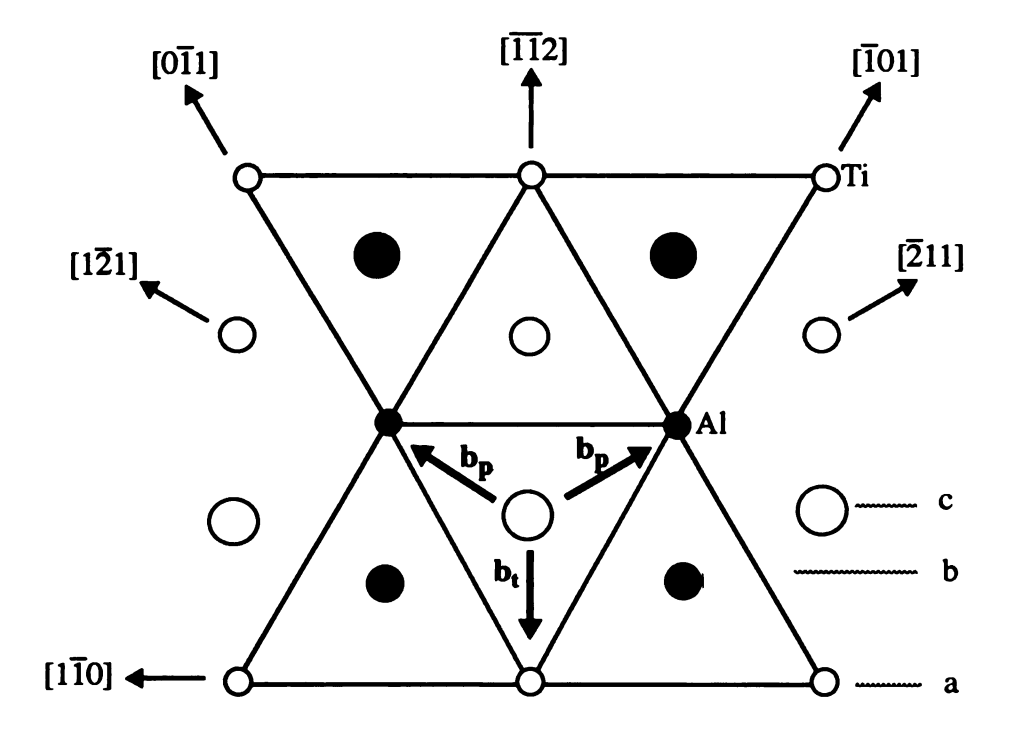
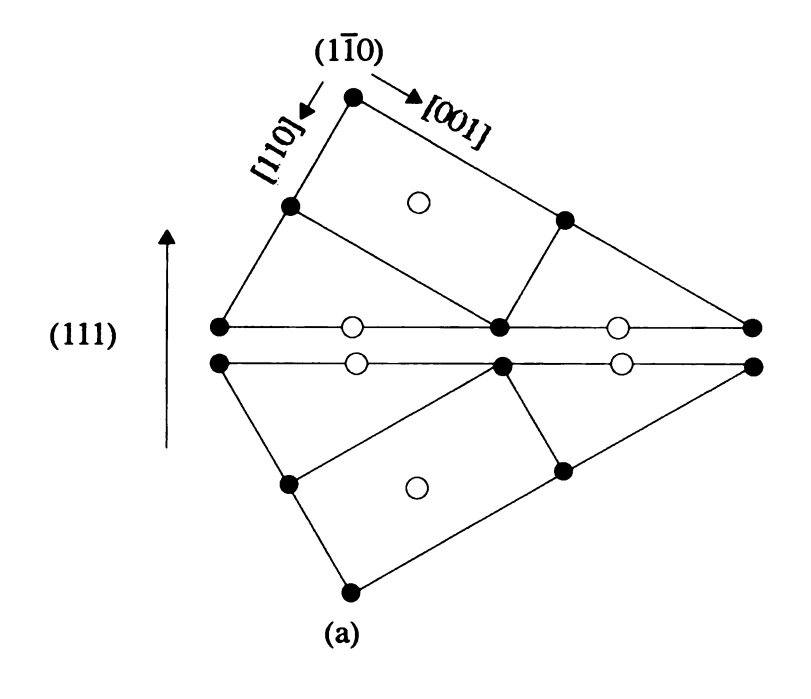


FIGURE 2.9. The atomic arrangement on the (111) plane, the layers labelled a, b and c define the abcabc... sequence along [111] ( $b_t$ : true twinning direction,  $b_p$ : pseudo twinning direction) [1].



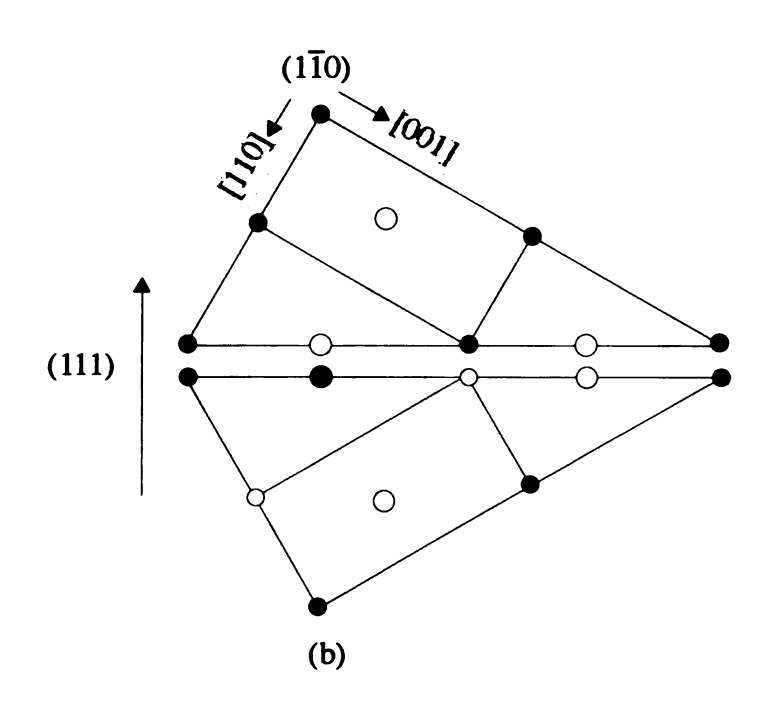


FIGURE 2.10. The atomic arrangement of true twinning (a) and pseudo twinning (b)

#### 2.3.3 Plasticity of TiAl.

Slip in TiAl occurs on {111} planes, as in f.c.c. structures. The possible slip directions are <110],<011] and <112]. The first systematic research on flow stress and ductility has been done by Schechtman et al. [44]. They reported that two major types of dislocations occur in TiAl: b=1/2[110] unit, perfect dislocations and b=[101], superdislocations. The first one is called the easy slip type dislocation and the latter one is called the hard slip type dislocation. This differentiation comes from the anisotropic L1<sub>0</sub> ordered crystal structure of TiAl which has tetragonality of 1.02 c/a ratio. Mechanical twinning also plays important role in the overall deformation. Lipsitt and Schechtman also reported that the deformation modes play different roles at elevated temperatures [24]. Following their results, the dominant slip mode at room temperature is the 1/2<110] easy slip type but as temperature increases, the <011] hard slip type, designated by superdislocation starts to contribute to the deformation considerably. So, they summarized that the mobility of the  $1/6[11\overline{2}]$  partial dislocation which is a constituent of the [011] superdislocation and is immobilized below 700°C, controls the plasticity of TiAl. However, the easy slip mode 1/ 2[110] dislocation has been called into question by Greenberg and co-workers [45,46]. They suggested that in the {110} planes filled with Ti atoms, the bonds, which are directed along both <110> and <001>, are covalent. The results of Court support this theory [47,48]. Thus, the Peierls stress caused by these covalent bonding blocks movement of 1/ 2[110] dislocations [49,50]. They concluded that the lack of ductility shown at room temperature of this alloy results from a lack of mobility of dislocations with b=1/2<110] caused by covalency, and the immobilization of dislocation with b=<011]. But, at higher temperatures, the increasing contribution of partial dislocation 1/6[112] and glissile

1/2[110] dislocation by thermal activation energy increase the ductility of TiAl. Kawabata and Vasudevan suggested that the purity and the existence of second phase Ti<sub>3</sub>Al could increase the ductility of TiAl [51,52,53]. That is, the phase Ti<sub>3</sub>Al absorbs the interstitial elements which increase the covalent bonds nature of Ti in TiAl, since the solubility of these elements in Ti<sub>3</sub>Al is much larger than in TiAl. So, the removal of interstitials from TiAl decreases the degree of directionality of bonding between the Ti atoms, and reduces the anisotropy in Peierls stress [54]. A duplex structure, which contains both single phase γ-TiAl and two-phase lamellar grains, is more ductile than a single phase or a fully lamellar structure. The deformation of this duplex structure occurs by primary twins and a/2[110] easy slip dislocations. Finally, the deformation modes may be controlled by anisotropic tetragonality, bonding, interstitial elements, grain size and grain boundary chemistry. So, the presence of second phases and the alloy composition are crucial factors that affect the ductility of TiAl [55].

#### 2.4 DESCRIPTION OF TEXTURE

#### 2.4.1 Definition of Texture

When non-random distributions of grain orientations occur by any kind of manufacturing process in materials, the orientation state of the grains is called texture. Significantly different texture can result from solidification, deformation, recrystallization and phase transformation.

#### 2.4.2 Eulerian Angles

Texture is described by two coordinate systems, the sample coordinate system and the crystal coordinate system. The sample coordinate system defines the three principal directions of the sample geometries and the crystal coordinate system defines the principal axes of the crystal orientation. The relationship is shown in Figure 2.11. The sample coordinate system and the crystal coordinate system can define a textured state by rotational angle vector  $\mathbf{g}$  represented by three Eulerian angles. The Eulerian angles are commonly defined using two variations, Bunge's system and Roe's system. The schematic view of each system is shown in Figure 2.12. The sequence of rotations for Bunge's system starts with the two orientation coordinate systems lying parallel to each other. Then, the crystal coordinate system (xyz) is rotated about the z-axis through the angle  $\mathbf{\phi}_1$  and the second rotation is done about the -x-axis through the angle  $\mathbf{\Phi}$ . Finally, by rotation of the crystal coordinate system about -z- axis through the angle  $\mathbf{\phi}_2$ , the rotational angle vector  $\mathbf{g}$  is defined by the three Eulerian angles  $\mathbf{\phi}_1$ ,  $\mathbf{\Phi}$ ,  $\mathbf{\phi}_2$ .

$$\mathbf{g_c} = {\{\phi_1, \Phi, \phi_2\}} = {\{g^z, g^{-x}, g^{-z}\}}$$
 (EQ 2.1)

In the case of Roe's system, the second rotation is not carried out about the x-axis, but about the y-axis. The Eulerian angles are represented by  $\Psi$ ,  $\Theta$  and  $\Phi$ .

$$\mathbf{g_c} = \{\Psi, \ \Theta, \Phi\} = \{g^z, \ g^{+y}, \ g^{-z}\}\$$
 (EQ 2.2)

Considering the fact that both kinds of Euler angles represent a same physical condition of material with different notations, they have a close relationship to each other. EQ. 2.3 shows the relationship between them [56].

$$\varphi_1 = \Psi + \pi/2; \ \Phi = \Theta; \ \varphi_2 = \Phi - \pi/2$$
 (EQ 2.3)

The third version of the Euler angle definition is the Kocks' system, which is employed in the present study. The Kocks convention is  $\Psi$ ,  $\Theta$ ,  $\phi$ . It is the same as Roe's except that the rotation axis is +z rather than -z for the third rotation. The sample coordinate system rotation from the crystal's perspective is obtained by the reverse order of rotations  $\mathbf{g}_{\mathbf{g}} = \phi$ ,  $\Theta$ ,  $\Psi$  about the opposite axes. Figure 2.13 shows the comparison of each orientation system.

In the representation of the Euler space, generally, two types of the Euler spaces are used. First one is the unit cell orientation space and the next one is the cylindrical orientation space. The Bunge's orientation system is well described by the unit cell orientation space, so called g-space and the Kocks' system operates the spherical orientation space. Figure 2.14 shows each Euler space.

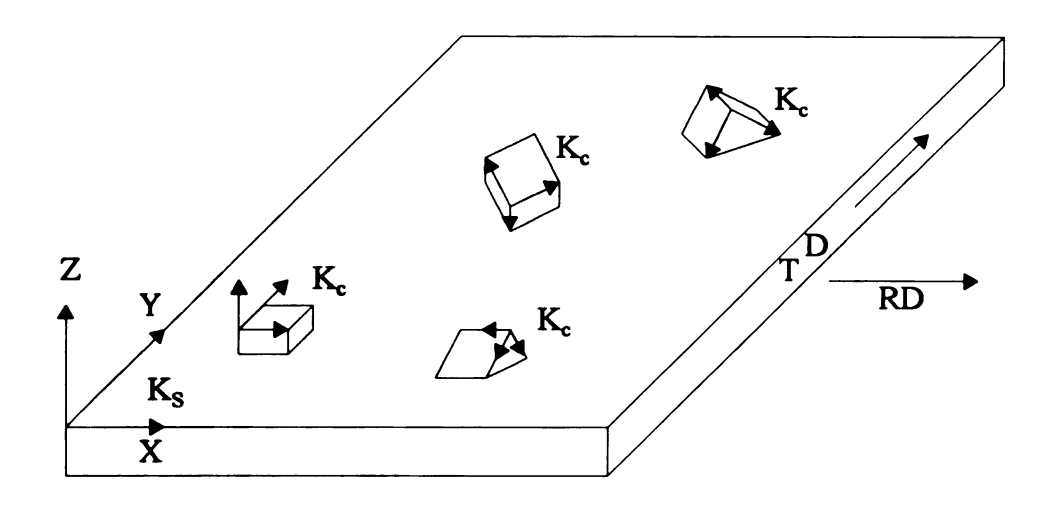
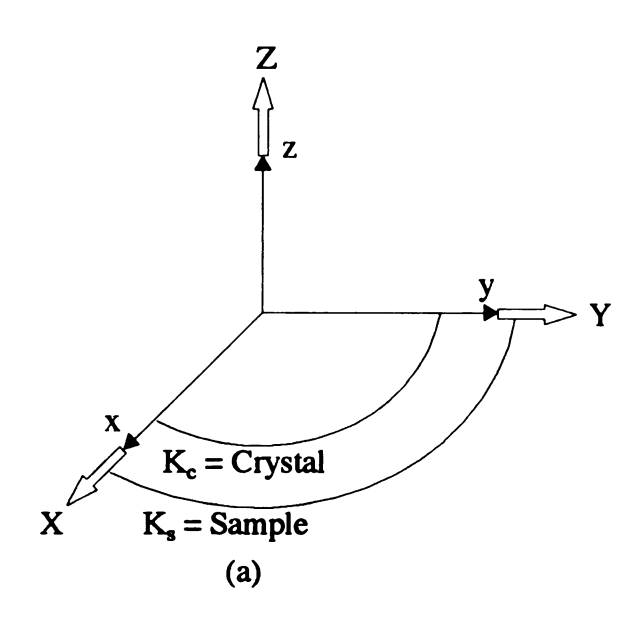


FIGURE 2.11. The sample fixed coordinate system  $K_s$  and the crystal fixed coordinate system  $K_c$  in the sheet [56].



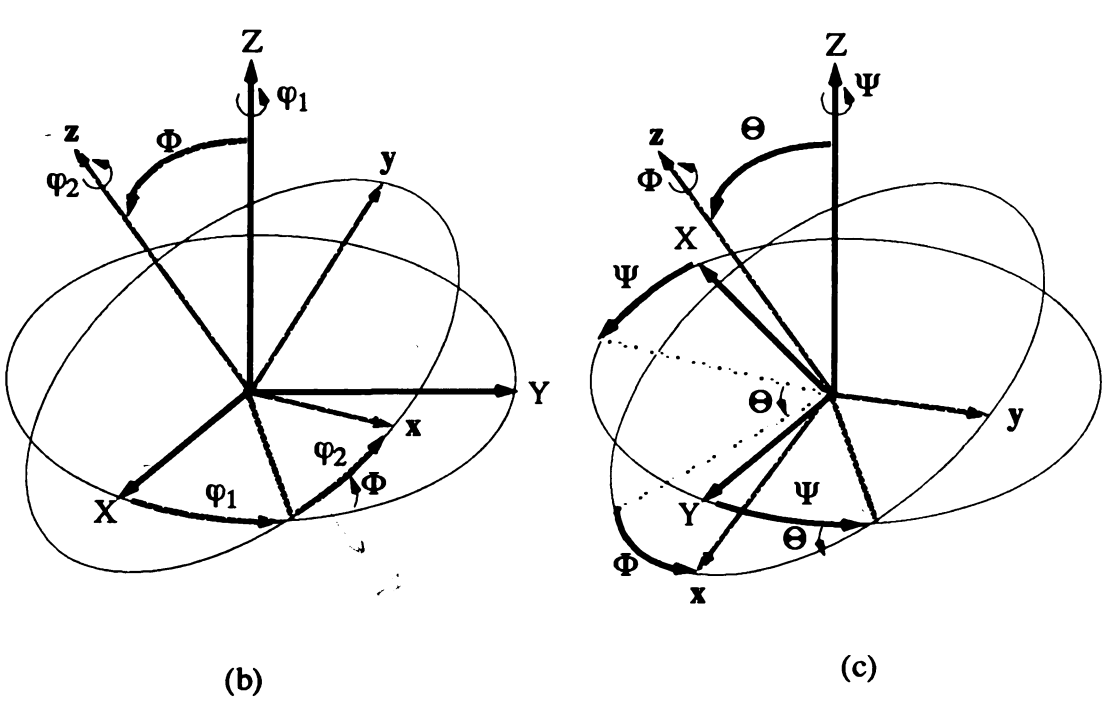


FIGURE 2.12. The definition of the Euler angles: (a) the crystal coordinate system  $K_c(xyz)$  lies parallel to the sample coordinate system  $K_s(XYZ)$ ; (b) on the definition of the Euler angles  $\phi_1 \Phi \phi_2$ ; (c) on the definition of the Euler angles  $\Psi \Theta \Phi$  [56].

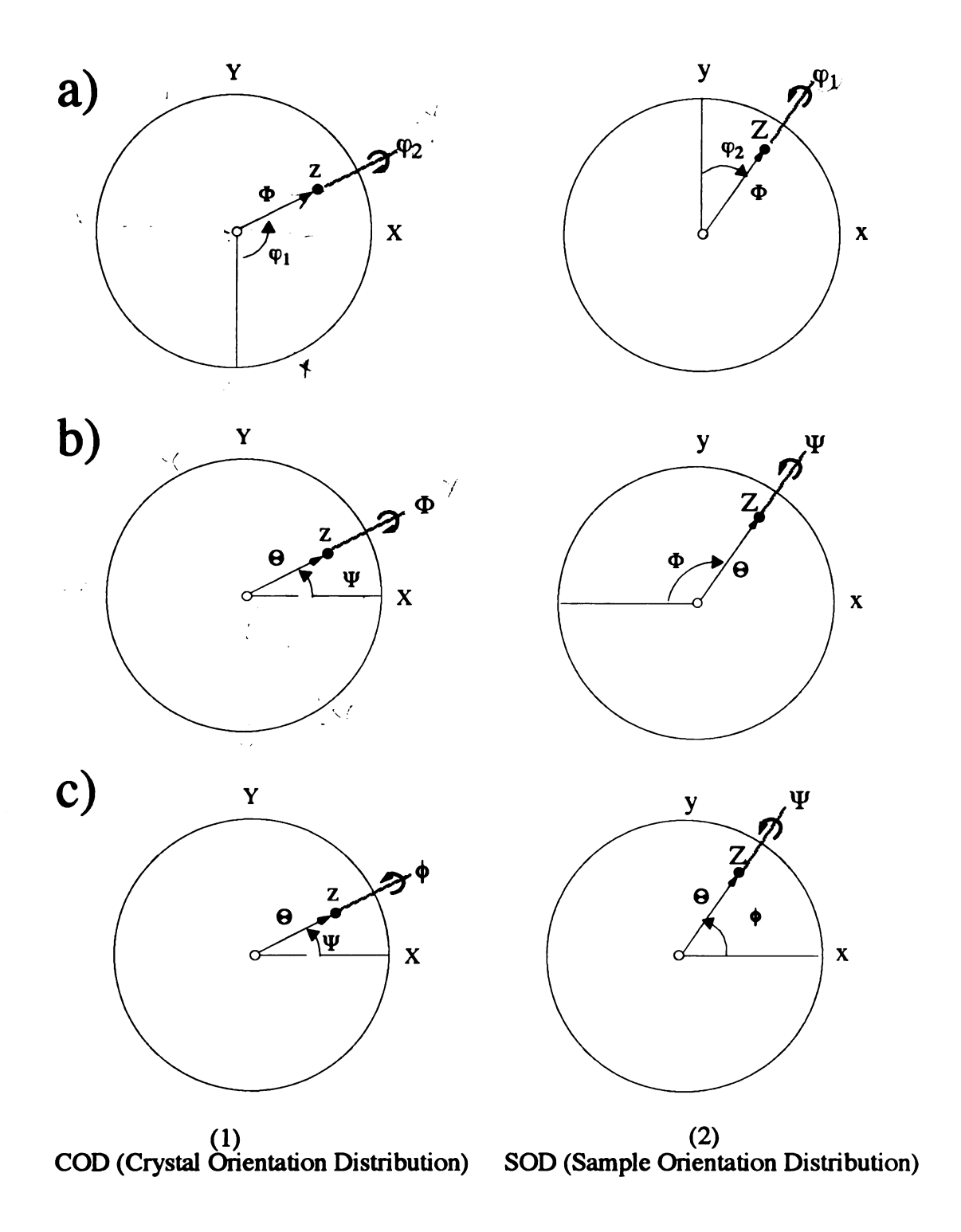
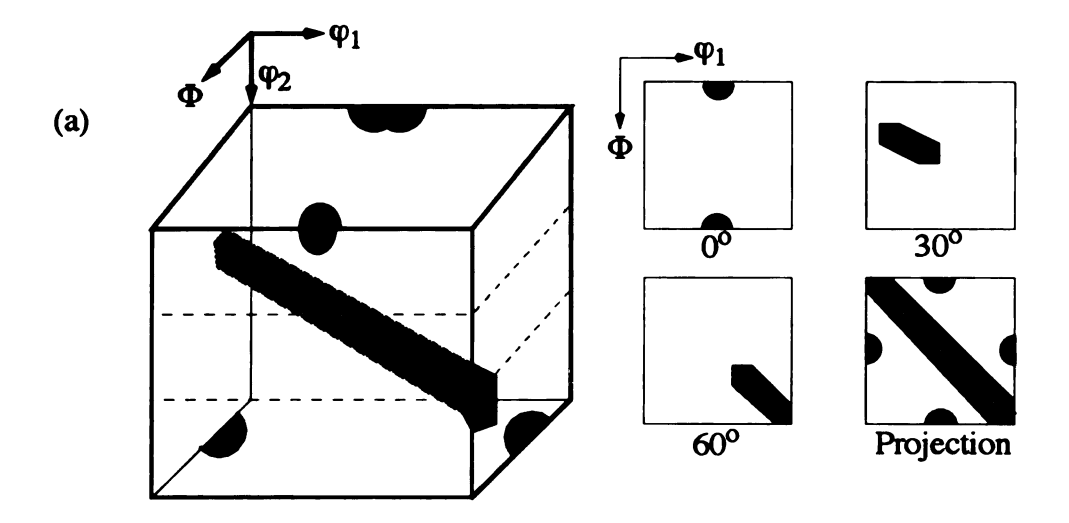


FIGURE 2.13. Euler angle rotations according to a) Bunge's system b) Roe's system c) Kock's system [57].



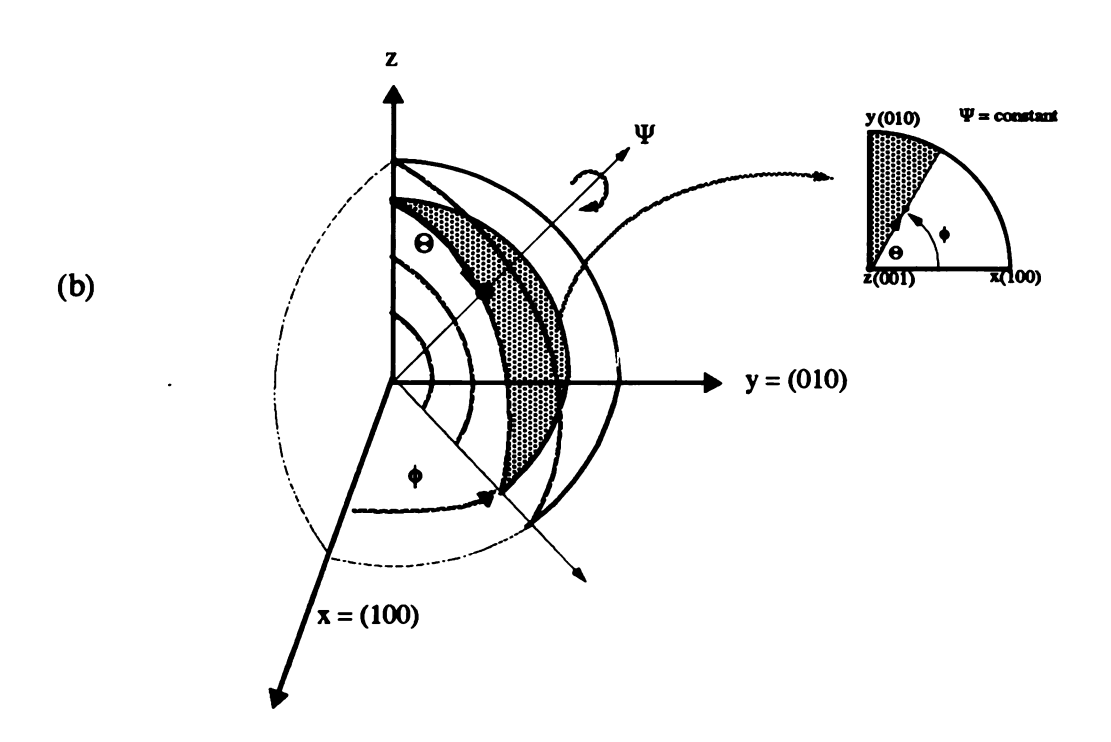


FIGURE 2.14. (a) Unit cell in Euler space (b) Spherical orientation space in Euler space, where Y can be viewed as the label for a shell having a particular rotation magnitude about the radial axis [58].

#### 2.4.3 Eulerian Angles and Miller Indices

Miller indices are commonly used to describe the crystal orientation with respect to sample orientation description. For example, in rolled sheet,

$$\mathbf{g} = (hkl)[uvw],$$
 (EQ 2.4)

(hkl) indicates the crystal plane which is parallel to the plane of the sheet and [uvw] indicates the crystal direction parallel to the rolling direction. It is also possible to obtain the relationship between the miller indices and the Euler angles by using a matrice conversion process [56]. The relation between the Euler angle representation and the representation of an orientation by Miller indices in terms of Bunge' system is:

$$\Phi = a\cos\frac{1}{\sqrt{h^2 + k^2 + 1^2}}$$
 (EQ 2.5)

$$\varphi_2 = a\cos\frac{k}{\sqrt{h^2 + k^2}} = a\sin\frac{h}{\sqrt{h^2 + k^2}}$$
 (EQ 2.6)

$$\varphi_1 = a \sin \left[ \frac{w}{\sqrt{u^2 + v^2 + w^2}} \cdot \sqrt{\frac{h^2 + k^2 + l^2}{h^2 + k^2}} \right]$$
 (EQ 2.7)

The relation in terms of Roe's system is:

$$\theta = a\cos\frac{1}{\sqrt{h^2 + k^2 + 1^2}}$$
 (EQ 2.8)

$$\Phi = a\sin\frac{k}{\sqrt{h^2 + k^2}} = a\cos\left[-\frac{h}{\sqrt{h^2 + k^2}}\right]$$
 (EQ 2.9)

$$\Psi = a\cos\left[\frac{w}{\sqrt{u^2 + v^2 + w^2}} \cdot \sqrt{\frac{h^2 + k^2 + l^2}{h^2 + k^2}}\right]$$
 (EQ 2.10)

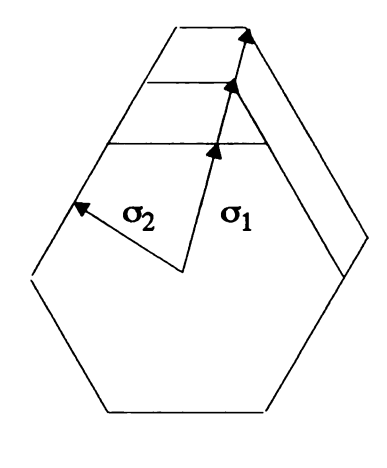
## 2.4.4 Pole Figures and Inverse Pole Figures

A two-dimensional representation of crystal orientation space is carried out using two approaches. The pole figure is the distribution of the specified crystal plane normals {hkl} with respect to the sample coordinate system in the stereographic projection. The inverse pole figure shows the distribution of crystal directions in a specified sample direction, such as the normal direction in terms of a crystal coordinate system, and it is expressed in a stereographic projection. For visualization purposes, the projection is often presented using an equal area net rather than the wulff net, so that the visual image does not contain any distortions.

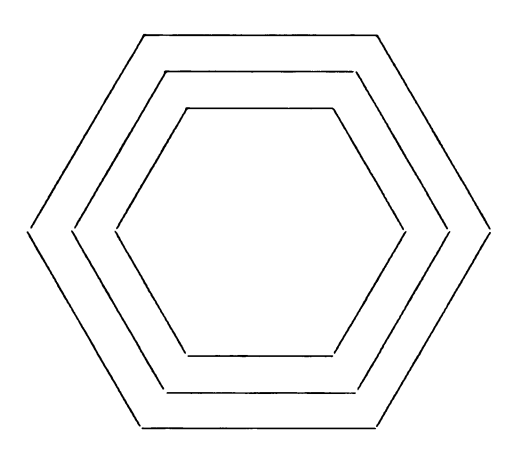
## 2.5 PLASTIC DEFORMATION OF POLYCRYSTAL

#### 2.5.1 Plastic Deformation in Polycrystal

The Schmid law requires that only resolved shear stress on slip plane and slip direction makes a crystal yield in a particular slip system. The fundamental idea of the plastic deformation of a polycrystal is such that simultaneous glide of dislocations in many slip systems in each grain are responsible for the deformation. In polycrystalline materials, it is not possible for each grain to deform by single slip or strain independently without being affected by the constraint of neighbor grains [59,60,61]. Taylor assumed that a slip in a grain in polycrystal requires five independent slip system and that each grain undergoes the same strain as the aggregate [62.63]. A macroscopic yielding behavior can be interpreted by an yield locus which can be represented by a polyhedron in 3-D stress space surrounding the origin [59]. A 2-D section through the origin of stress spaces reveals a polygon, as shown in Figure 2.15. In the yield locus, each facet indicates the criteria for yielding on each slip system. When a resolved shear stress reaches a yield surface of a specific slip system, the minimum condition for yielding is satisfied. But, as mentioned above, in polycrystal deformation, at least five slip systems are required. Therefore, only a single yield criteria is insufficient for polycrystal slip. At a corner orientation on the yield locus, several slip systems can be activated simultaneously. This indicates that for polycrystal yielding, each grain orientation should rotates to meet such a yield corner that can produce poly slip conditions [64,65,66,67].



(a) None



(b) Isotropic

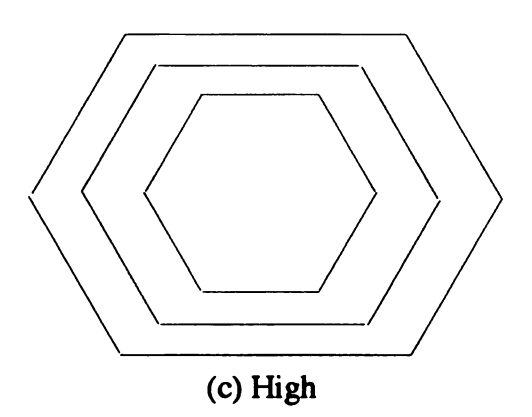


FIGURE 2.15. 2-D Yield Locus and Latent hardening [59]

#### 2.5.2 Formation of Deformation Texture

The formation of deformation texture starts with such considerations. Figure 2.16 shows that an orientation rotates due to a given stress state indicated by a e u b w p q [68]. The arrows I and II indicate the rotations resulting from single and duplex slip respectively. In the stress axis rotation which follows a minimum resolved shear stress, single crystal slip occurs when the path of the stress axis lies within a unit triangle and duplex crystal slip occurs when the path is along the unit triangle boundary. The final rotation is determined by the competition between these two slip systems.

Figures 2.17-18 show the general trends of rotation in copper and  $\alpha$ -brass under tension. For tension in FCC structures, the final texture components are [111], [100] and [112] and for compression, the final components are [110] with a spread toward [311] and [100] for copper and toward [311] and [111] for brass. The characteristics of deformation texture in FCC mostly result from the comparison between copper type texture and  $\alpha$ -brass type texture. The difference comes from the operation of latent hardening in each case, which is illustrated in Figure 2.15. There are two assumptions in the description of latent hardening [59,69,70]. First, the latent slip systems do not harden at all or they harden at the same rate as the primary slip system. In second case, the latent slip systems harden faster than the primary slip system. For the  $\alpha$ -brass case, when the latent hardening exceeds the active hardening, the [100] component disappears. Figure 2.18 shows the general trends of rotation in copper and in  $\alpha$ - brass under compression.

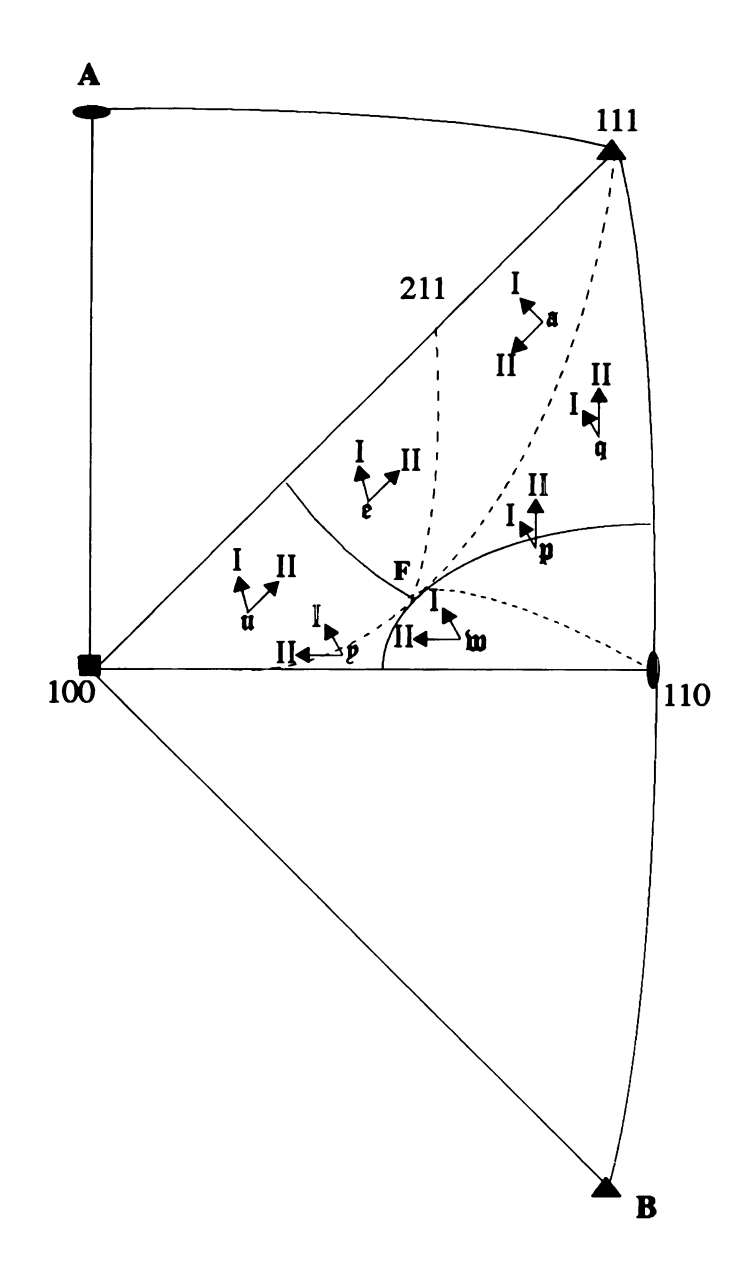


FIGURE 2.16. Lines of maximum descent from the point of maximum resolved shear stress F and directions of rotation due to single crystal slip  $(\rightarrow I)$  and duplex slip  $(\rightarrow II)$  in copper under tension [68].

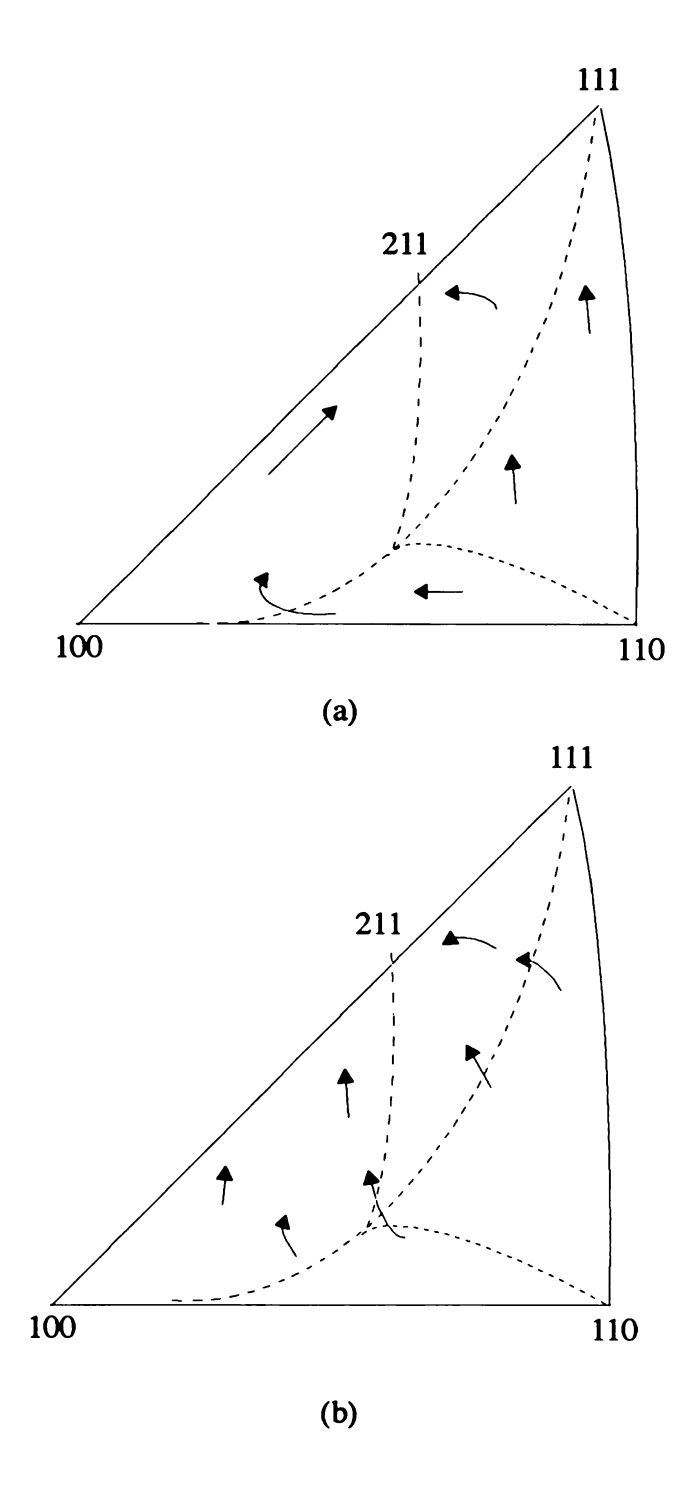


FIGURE 2.17. (a) General trends of rotation in copper under tension (b) General trends of rotation in  $\alpha$ -brass under tension [68]

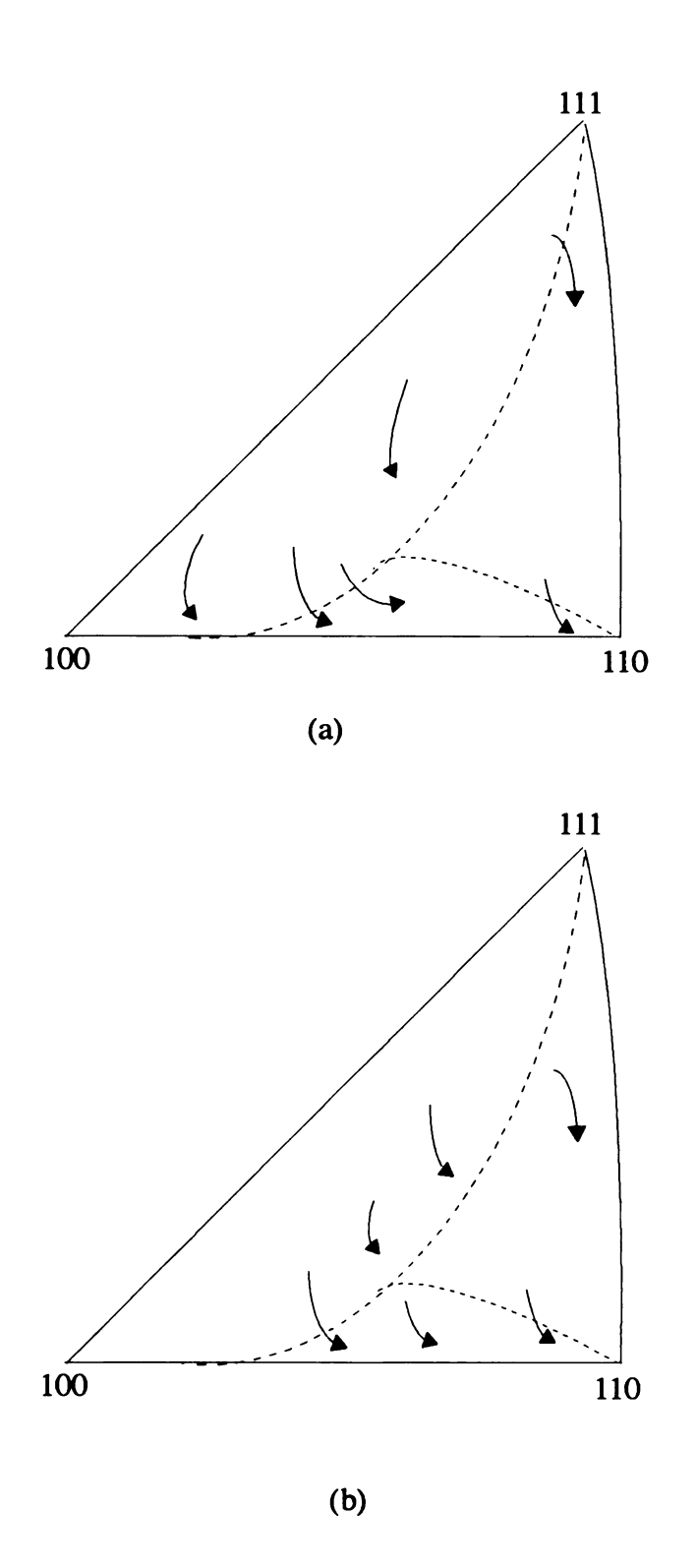


FIGURE 2.18. (a) General trends of rotation in copper under compression (b) General trends of rotation in  $\alpha$ -brass under compression [68].

As descriptions of deformation textures, drawing texture and rolling texture are used frequently [68,71,72,73]. The process of wire-drawing is such that a tensile stress is applied in the direction of drawing together with compressive stresses in all radial directions perpendicular to the tensile direction. Thus, texture forms on the basis of the tension rotation which leads to [111], [112] and [100] in the drawing direction, simultaneously with compression rotation with respect to radial direction. In a  $\alpha$ -brass, the [100] component disappears due to latent hardening. In the case of the sheet rolling texture, the process is described by compression parallel to the rolling plane normal and tension in the rolling direction perpendicular to the rolling plane normal. Thus, the polycrystal aggregate is interpreted by compression axes all over the triangle [100][110][111] and tension axes all over the area 90 degrees from this triangle. The final rolling textures are {4.4 11}<11.11.8> for copper and {110} <112> for brass.

#### 2.5.3 The Effect of Stacking Fault Energy on Deformation Texture

In FCC materials, the composition can affect the overall plastic deformation behavior, which is affected by materials of different stacking fault energy. For high SFE (Stacking Fault Energy) materials such as gold and copper, cross-slip is possible. This mechanism indicates that dislocation segments which are all {111}<110> slip system pairs in f.c.c. materials can move from its slip plane on to an intersecting slip plane sharing a common slip direction (colinear slip). In aluminum the dislocations cross-slip easily, even at relatively low stress levels [74]. But, this homogeneous slip theory does not take into account deformation inhomogeneities which usually occur in medium and low SFE materials such as Cu-Zn alloy. The deformation inhomogeneities are caused by deforma-

tion bands, shear bands (consequence of latent hardening) and also, mechanical twinning [75].

In the case of twinning, since mechanical twinning causes a drastic orientation change from that of the matrix, it is expected that mechanical twinning plays an important role in the development of deformation texture. For the plane stress state, occurrence of mechanical twinning is determined by the Schmid factors  $\mu_t$  for {111}<112> twin deformation and by  $\mu_s$  for {111}<110> slip. If  $\mu = \mu_t / \mu_s$  is larger than one, mechanical twinning occurs assuming that CRSS is the same. In the case of Cu-Zn system, the orientation described by the {112}<111> which is called C- orientation develops during the initial rolling. With further rolling, the material undergoes mechanical twinning, so the final component is the {552}<115> TC (twinning copper orientation). The procedure to find the twinned orientation with respect to the initial orientation will be explained in section 6. Hirsch and Lucke showed that increasing Zn in Cu-Zn system and increasing deformation decrease the C-orientation, but increases the G-component {111}<001> which is near the TC orientation [76]. The generation of the G-component is caused by a subsequent slip of the TC orientation after twinning. For high Zn Cu-Zn system, mechanical twinning occurs after a much smaller strain, compared to the low Zn case. These results indicate that the transition from the high SFE condition of pure copper to the low SFE condition of Cu-Zn by adding Zn not only increases the generation of mechanical twinning but also decreases the critical strain which is necessary for mechanical twinning to occur. Figure 2.19 shows the orientation paths due to mechanical twinning of {112}<111> and subsequent deformation.

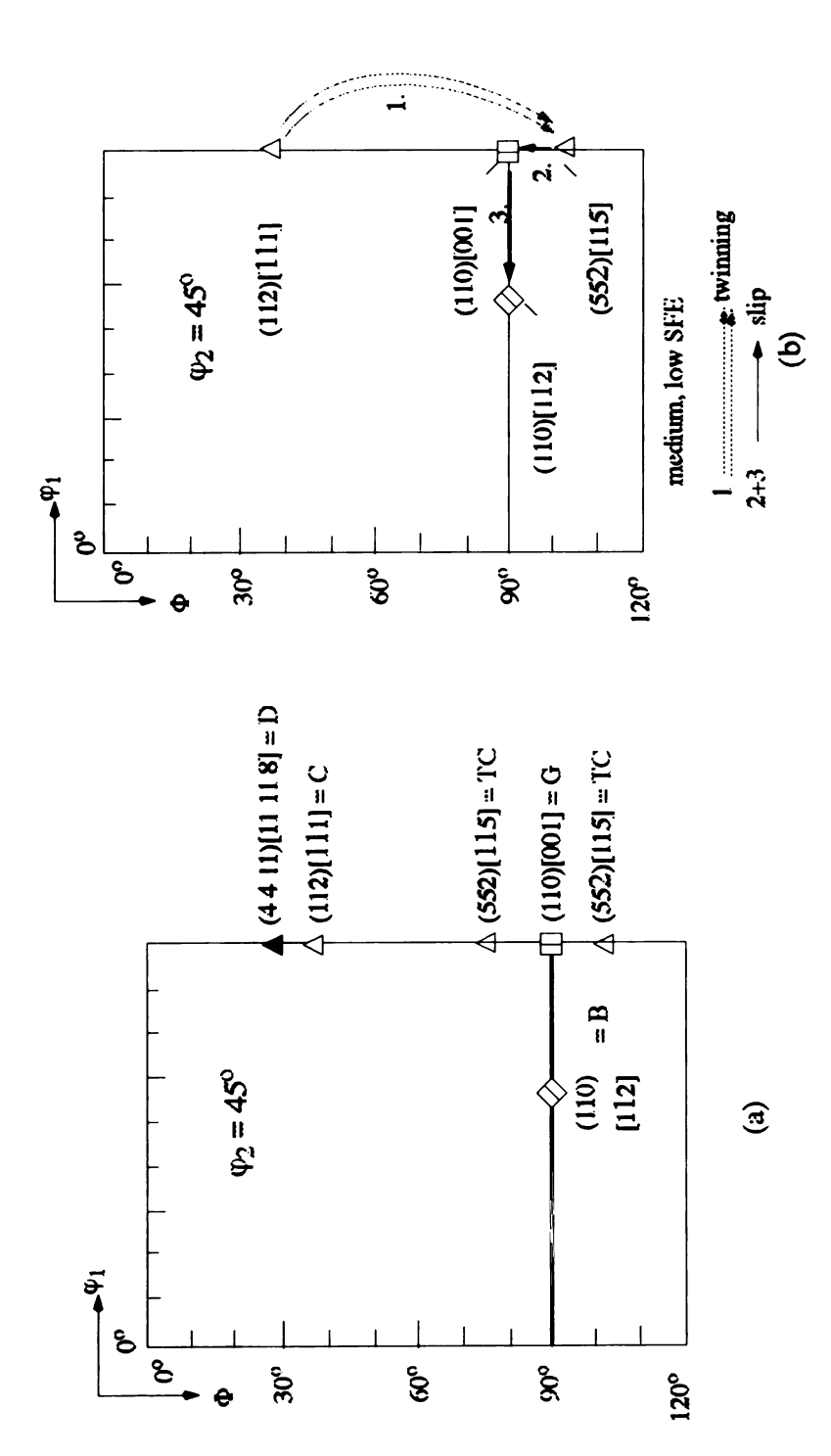


Figure 2.19 (a) Formation of Copper rolling orientation D by initial rolling deformation and deformation in the  $\varphi_2 = 45^{\circ}$  section of the Euler space of the Bunge's system [76]. (b) Orientation paths due to mechanical twinning of {112}<111> and subsequent

# 3. EXPERIMENTAL PROCEDURE

## 3.1 SPECIMEN PREPARATION.

The purpose of this experiment is to investigate the deformation mechanisms of gamma-based TiAl alloys at room temperature and elevated temperatures. The material used in the present work was investment-cast near-gamma Ti-46Al-2Cr-2Nb (at%). The chemical composition is shown in Table 3.1. The material was supplied in the form of a rod ~18 mm in diameter and about 100 mm long by Howmet Corp., Whitehall, MI. The material had been hot isostatically pressed (HIP'ed) and heat treated to form a duplex microstructure. The duplex microstructure consists of approximately equal fractions of equiaxed gamma, and  $(\gamma + \alpha_2)$  lamellar grains, which were transformed from alpha single phase during heat-treatment process.

Table 3.1 Chemical composition of specimen

Ti	Al(at%)	Nb(at%)	Cr(at%)	O(ppm)	N(ppm)	H(ppm)
	46.3	1.9	1.6	510	49	20

TiAl shows higher strength compared with most steels commercially used in machining tools. Thus, the preparation of specimens required use of a diamond saw and EDM (Electron Discharge Machining). First, the cast circular rod was cut into a quarter section having a 7.6 mm radius. A diamond saw was used to section this quarter section specimen into several pieces with 10 mm height. All cuts were perpendicular to the sides

to reduce the possibility of shear strains during the uniaxial compression. Due to experimental difficulties which will be described in the next section, the cross sectioned area of the quarter-specimen was cut into three pieces having 15 mm<sup>2</sup> area in each piece shown in Figure 3.2, and the height was also reduced to 5 mm, half of the size of the original height. This was done by EDM because of the lack of ability to maintain accuracy with a diamond saw.

### 3.2 EXPERIMENTAL PROCEDURES FOR COMPRESSION TESTS

#### 3.2.1 Compression test system

The equipment used for compression tests was an ATS series 2710 creep testing machine and the compression data were recorded by a data acquisition system developed by Wu [77]. The machine has a lever arm ratio of 20:1 to provide high load capacity and loading rate. The frame controller made by ATS (Applied Test systems INC.) and EIR (Electric Instrument Research Corp.) provides signal processing and feedback control for various kinds of experiments. The compression tests were conducted by imposing a constant velocity on the lever arm with the jack shown in Figure 3.1. The compression specimen was put on Inconnel loading platens inside a compression cage. The displacement of the specimen was measured by LVCT (Linear Variable Capacitance Transducers) that monitored the change in distance between the upper and lower surfaces of the compression cage. The function of LVCT is to convert the physical displacement to an electrical voltage change. The load was measured with a load cell in the lower end of the load train. The LCVT and load cell signals were conditioned to provide output voltages that were

monitored by the data acquisition board of a computer which consists of IBM PS/2 286 computer and AT-MIO-16L-25 multifuction data acquisition board. The LCVT exhibited a range of -10 to 10 volts for a displacement of 5.08 mm (0.2 in.). The experiment started in a negative voltage of about -7 V and the voltage increased as the specimen was compressed. The resolution limit in the data acquisition system was about 5mV (1  $\mu\text{m}$ ,  $5\times10^{-5}$  in, or 250  $\mu\text{e}$ ). The testing temperature was controlled by an ATS furnace control unit. The furnace has three heating zones. Thus, the furnace control unit allows the user adjust the temperature profile in the range of the specimen. The temperature was monitored at the top and bottom of the loading platens and adjustments in the heating zones were made to keep the specimen within  $\pm$  2 °C fluctuation range.

## **3.2.2** Compression test procedures

The geometrical complexity of the specimen and the testing machine required measurement of the compliance for each experiment condition. Figures 3.3-3.5 show the comparison between the compliance curve and the compression curve for the specimen at each temperature. After each compression test, the stress-strain curve was obtained by substracting the compliance curve from the data. The first experiment was done at room temperature, and it is illustrated in Figure 3.3

In using the creep tester for the compression experiment, one problem arose during the first room temperature experiment, which occurred using a specimen with a full quarter section of the cross sectioned area of 45 mm<sup>2</sup>. The thread failed in one of couplings in the load train made from a mild steel due to the high yield stress of TiAl. This failure led

to reducing the loaded area of the specimen to one third of the original specimen size. The area reduction of the stress area in the specimen was determined by the thread design analysis and the yield stress analysis of each material used in the testing machine and specimen. The thread design analysis follows the Dimension of Unified and American National Screw Threads (DNAT) [78]. In the stress distribution on the threads, the major portion of the load is transferred at the first pair of contacting thread and a large stress concentration is present here. Stress concentration factors for threads with static loads are usually determined by photoelastic analysis and it is reported that a stress concentration factor is 3.85 at the root of the first engaged thread.

$$MS = CF \times \frac{AL}{SA}$$
 EQ. 3.1

In EQ. 3.1, the Maximum Stress (MS) on the first thread is calculated by the stress concentration factor (CF), applied load (AL) and stress area (SA). And the stress area (SA) is obtained by the thread size and the number of threads per inch. Therefore, by comparison between the maximum applied load of the testing machine, the yield strength of the thread material, in the coupling, and the yield strength of TiAl, the criteria for loading condition can be determined. In this experiment, the yield strength of TiAl at the room temperature was estimated to be 500 MPa and with that stress, the applied load had to be about 5000 lb.. in the loaded area of specimen which was a quarter section of the circular area with 7.6 mm radius. The thread size used in the coupling was 3/8"-24-2A. So the stress area in the thread was 0.0878 in<sup>2</sup> which is indicated in the DANT. Thus, the maximum stress on the first thread was about 400 MPa by EQ. 3.1 and this value was about two times of the yield strength of mild steel. Therefore, it was necessary to reduce the loading

area in the specimen, and the area was reduced to 1/3 of the original size shown in Figure 3.2. The specimen was fit into the specimen holder in the compression cage in order to get uniaxial compression state. The specimen was sprayed with boron nitride to prevent frictional damage and diffusion effects between the specimen surface and compression cage during high temperature compression.

The experiment was conducted under as shown in Figure 3.1 constant displacement rate condition. The strain rate was nominally  $4.4 \times 10^{-5}$  s<sup>-1</sup>. The experiment was conducted in two environments. Room temperature tests were done in laboratory air. At higher temperatures, the testing condition was in a flowing Ar atmosphere in order to reduce oxidation of the TiAl. In the high temperature experiments, each specimen was kept at the test temperature for 20 minutes to homogenize the temperature before the compression test. The testing temperature was held constant. The final strain after each test was obtained from the thickness and cross sectional area change before and after compression. Practically, a pre-loading condition was applied in each test to maintain continuity in the load train. It also influenced each stress-strain curve by shifting the origin of the strain axis to the left. The direct comparison between the stress-strain curve and the measured specimen dimensions indicated a lower strain than recorded in the stress-strain data, by about 0.02 ε. The difference may be due to lubrication and deformation in the platens. The first room temperature test caused an indentation in the Inconnel loading platens. The loading of the platens in the subsequent compliance test caused a reversed strain in the platens as illustrated in Figure 3.3. Consequently the stress-strain curve at room temperature is not completely accurate. All these effects are illustrated in Table 3.2 and Figure 3.6 where the load displacement data are converted to engineering stress-strain curves.

Table 3.2 The order of experiments and conditions of each test.

Temperature	Shape	ε <sub>d</sub> , ε <sub>m</sub>	Comments
room temp.	$\Box$	0, 0	thread failure in couplings
room temp.		5.5%, 8.3%	dents were formed in platens
room temp.			compliance test: dents partially removed
850°C	Δ	2.9%, 4.8%	
850°C			compliance test
room temp.		3.3%, 5.6%	lost 2 pole figures before compression
room temp.			compliance test
650°C		5.9%, 8.2%	
650°C			compliance test
room temp.		NA, 9.7%	lost load-displacement data

<sup>\*</sup>  $\epsilon_d$ : strain obtained from data,  $\epsilon_m$ : strain measured from specimen

#### 3.3 TEXTURE MEASUREMENT

#### 3.3.1 Texture measurement

The texture measurements were carried out with a Scintag diffractometer, SDS-2000, which has a computer controlled four axis rotation system with no slits and a 1 mm collimator. For a precise measurement before and after deformation, the specimen center was mounted and aligned as accurately as possible in the specimen holder as shown in Figure 3.2 (b). For the determination of textures in the  $\gamma$ - phase, the following incomplete pole figures were measured using Cu K $\alpha$  -radiation: {111}, {200}+{002}, and {220}+(022}. The L1<sub>0</sub> structure of TiAl is a tetragonal, fcc-related, ordered structure with

a c/a ratio close to unity (c/a = 1.02). Thus, X-Ray reflections originated from the lattice planes in the same group with slightly different d-spacings. The separation of two close peaks is possible using appropriate slits and a monochromator. In this experiment, no attempt was made to separate the reflections. The superlattice reflections (001), (110) were not utilized in this experiment because of their low intensity.

The intensity for a given pole figure was obtained at  $5^{\circ}$  increments in azimuthal rotation,  $\phi$ , up to  $360^{\circ}$ , and with  $5^{\circ}$  tilt increments of  $\chi$  up to a maximum tilt angle of  $80^{\circ}$ . The scanning time at each increment of azimuthal angle was set at 4 sec. which provided a sufficient intensity.

The grain size distribution of the specimen was obtained by J.Sadowitz [79]. Following his analysis, the majority of equiaxed grains were in the 1000 square microns to the 4000 square microns size range and the spatial distribution of grains was quite random. Some grain sizes were 8000 square microns. The lamellar grains were much lager than equiaxed grains in grain size. The exposed area by X-ray beam was about 3.8 mm<sup>2</sup>. This implied that at about 600 equiaxed and 150 lamellar grains contributed to the texture measurement.

## 3.3.2 Procedures in using popLA

Texture data reduction in this experiment was carried out with Scintag XDS, a software, a pole figure measuring code entitled SCIN5A and the software popLA (Preferred Orientation Package from Los Alamos, Los Alamos National Laboratory) [80]. The steps used in measuring texture are;

- 1. Measure 2-theta angle with a command C:\POLEFIG SCIN5A ... Here, the user can do omega(theta) or chi scan. The purpose of the 2-theta scan was to determine the peak and the width of the peak so as to identify 20 positions to measure background intensity. The number of 2-theta measurements depends on how many poles are required in the experiment.
- 2. Start measuring pole figures. In this step, the user decides the number of poles, scanning time and the maximum tilt angle ( $\chi$ ). Considering the geometrical limitations of defocusing of the X ray beam on an highly tilted surface, the maximum tilt angle is limited to  $80^{\circ}$ .
- 3. After measuring pole figures, data are stored in a file named <FILE-NAME>.RAW.
  - 4. Run popLA with a command c:\x popla \( \daggered{1}\).
- 5. Make DFB file. The .DFB (defocusing and background) file contains information necessary for popLA to estimate a correction for geometric defocusing and background X-Ray intensity. The program requires a slit size to compute the correction file and the value supplied was 1 mm. A 1mm collimator is used in the pole figure measurement instead of normal slit. The collimator size is determined by the diameter of the circular shape of the tip of the collimator. The DFB file corrections are only approximate, and not calibrated for the machine, but they do give a systematic correction that permits meaningful comparison.
- 6. Make EPF file. With the .DFB file, the raw data file is normalized and the output file is named <FILENAME>.EPF (Experimental Pole Figure). With the EPF file, the user can visualize the pole figure on the screen and print it out.

- 7. Complete pole figures using spherical harmonics. The outer rim of the experimental pole figure is estimated. This permits a more accurate normalization of the pole figure.
- 8. Compute the sample orientation distribution (SOD). The WIMV algorithm is used and file named <FILENAME>.SOD is created. As discussed in the section 2, the description of SOD or COD (crystal orientation distribution) is determined by the relationship between sample coordinate system and crystal coordinate system. Thus, it is necessary to specify the symmetry of sample coordinate system (orthogonal) and the crystal coordinate system (cubic).
  - 9. Calculate Inverse Pole Figures from .SOD. The file extension is WIP.
- 10. The files with extensions like EPF, SOD and WIP can be visualized and printed out in the form of two dimensional graphic image using the program POD.
  - 11. Save a image using a conventional image capturing program (HiJET Pro).

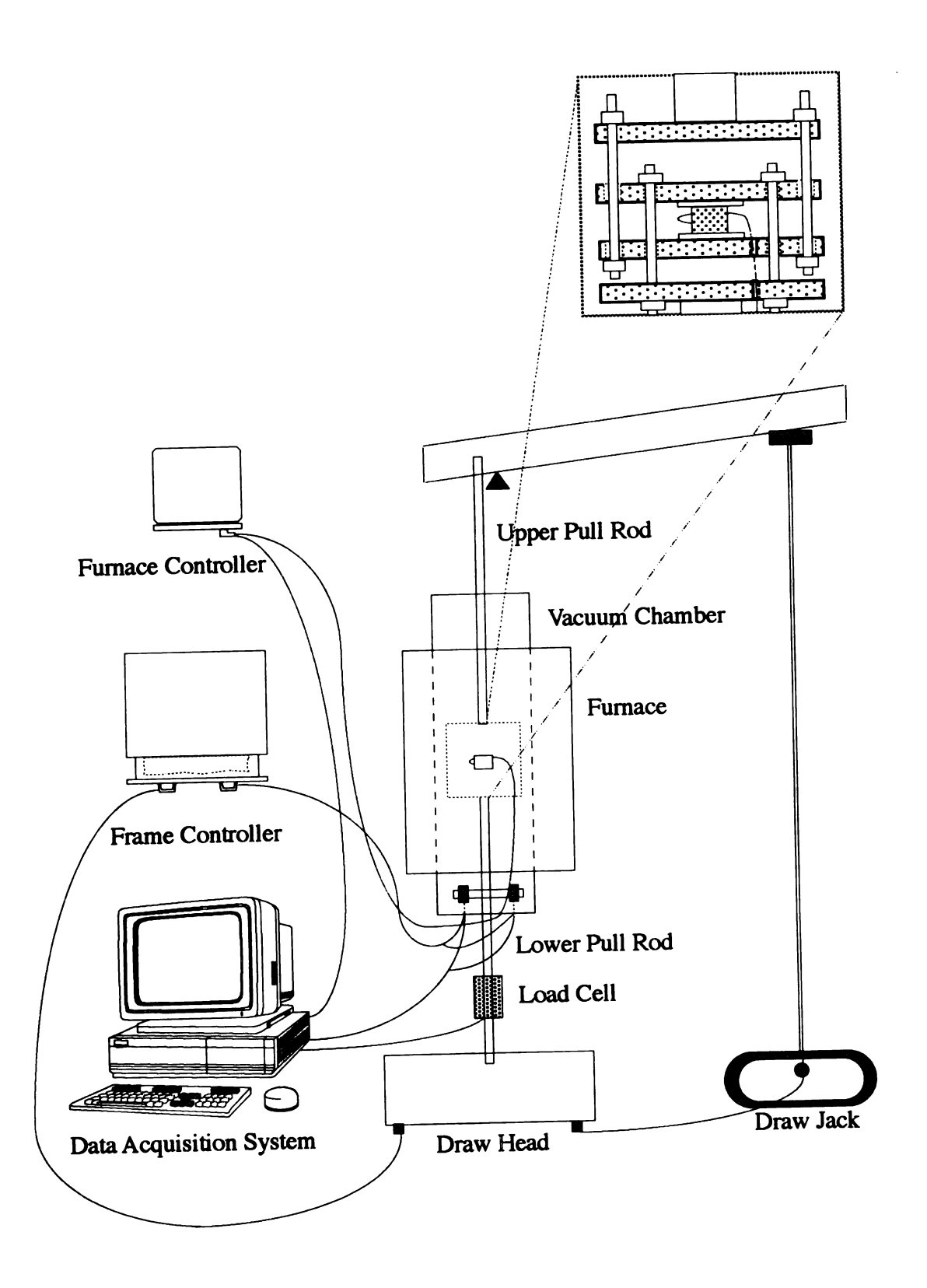


FIGURE 3.1 Schematic view of the compression system

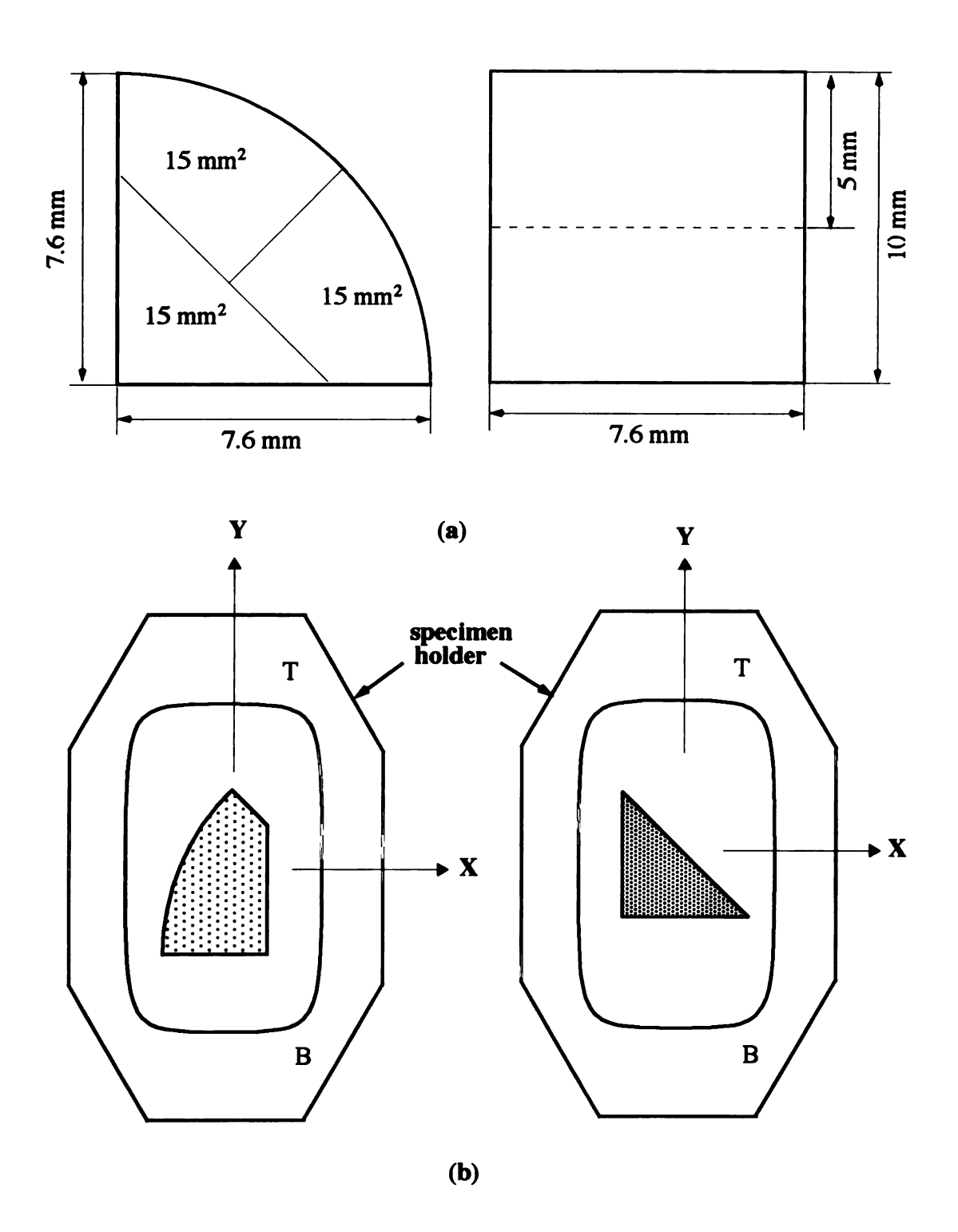


FIGURE 3.2 (a) Shape of specimen (b) specimen orientation in the specimen holder for the pole figure analysis

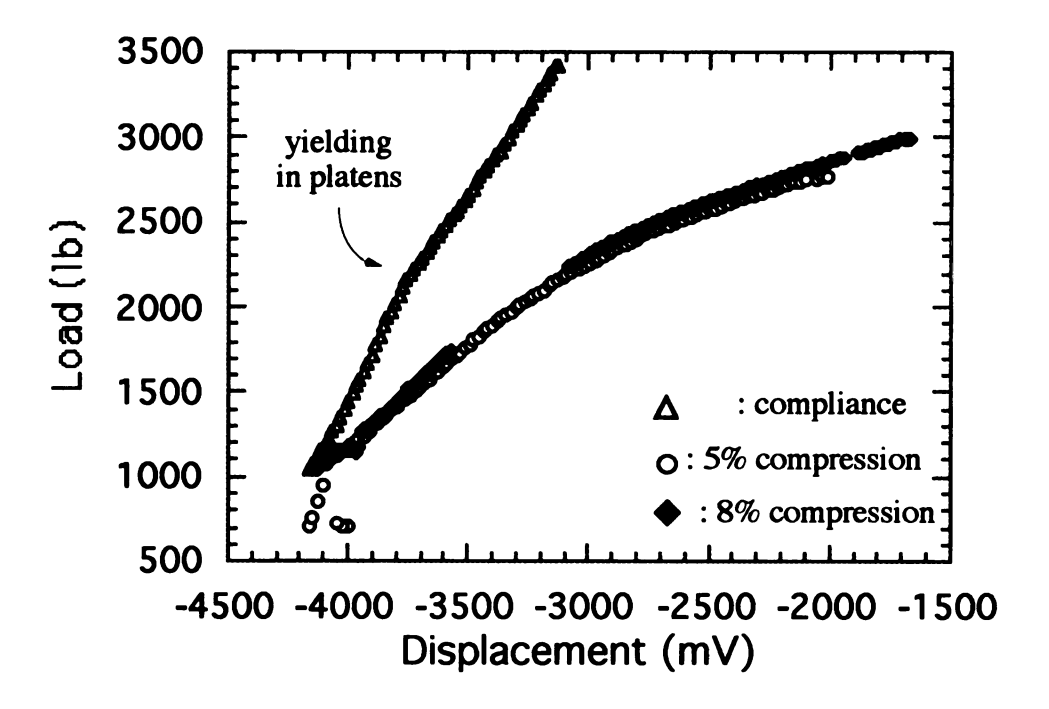


FIGURE 3.3 Comparison between compliance and compression curve at room temperature

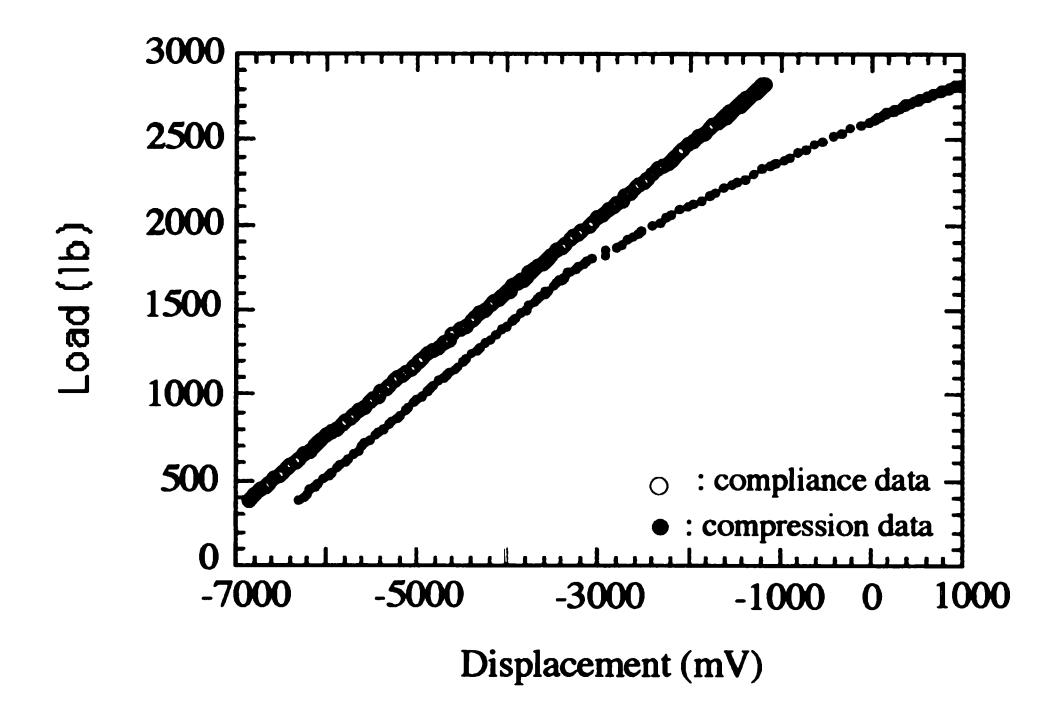


FIGURE 3.4 Comparison between compliance and compression curves at

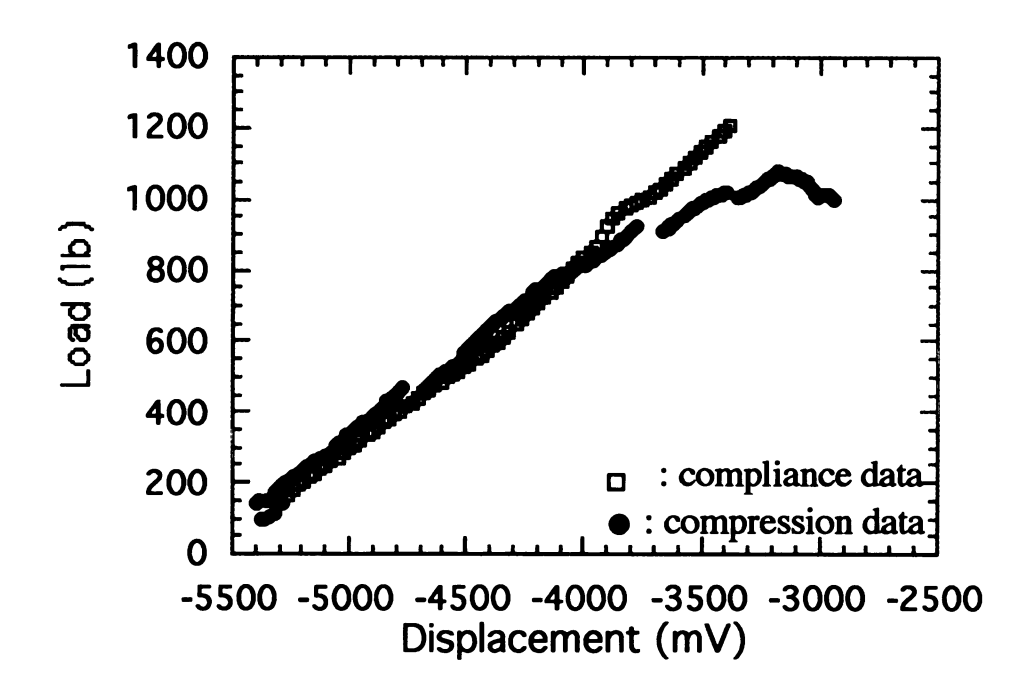


FIGURE 3.5 Comparison between compliance and compression curves at

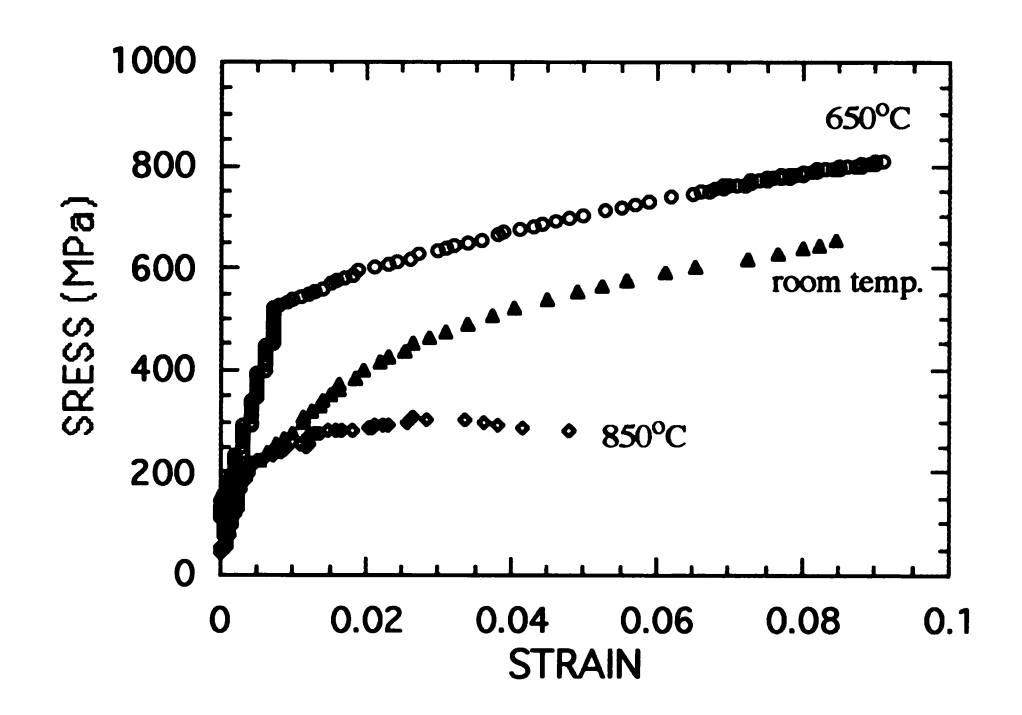


FIGURE 3.6 Stress-Strain curves at each testing temperature after deforma-

## 4. RESULTS

#### 4.1 STRESS-STRAIN BEHAVIOR

Figure 3.6 shows the engineering stress-strain curves measured at three temperatures at the strain rate of  $4.4 \times 10^{-5} \, s^{-1}$ . At  $850^{\circ}$ C, the curve starts to show the work softening effect just after peak stress about at  $\epsilon = 0.3$ . But, for the two lower temperature experiments, the work softening effect is not detected. The gaps in the strain record at  $850^{\circ}$ C resulted from the slowness of the computer when it was storing data to disk. The lower temperature samples exhibited work hardening throughout the strain range. In these experiments, the final strain was after strain of 5~8%. The curve at the room temperature shows a lower slope in the elastic region. The optical microscopic observation indicated many cracks in the room temperature experiment. The strain obtained at room temperature in inside specimen was 8.3%. The curves at  $650^{\circ}$ C and  $850^{\circ}$ C show a consistency in the elastic region, and the final strains were 8.2% and 4.8% respectively.

#### 4.2 TEXTURE AFTER COMPRESSION

#### 4.2.1. Texture at room temperature

Figure 4.1 shows (111) pole figures which include the undeformed state and the deformed case. In the undeformed case, the distribution of high intensities of (111) poles appears randomly distributed. However, the strongest and largest group of (111) poles are observed in the vicinity of  $\Theta = 30 \sim 40^{\circ}$ . After compression, the poles which existed individually in the undeformed state, appear to be clustered, which indicates a more strongly textured state. The strong clusters are observed around  $\Theta = 35^{\circ}$ . Even though the strong (111) poles were already situated around  $\Theta = 30 \sim 40^{\circ}$  before compression, the pattern of their existence was spike-like single peaks. But the characteristics of poles after compression indicate that they were more grouped after deformation, following the compressed state. Figure 4.3 shows (220) pole figures before and after compression. The clustering phenomena are also observed after compression in the same manner as the (111) pole figures. The strong component is located around  $\Theta = 0^{\circ}$  after compression. The (200) pole figures are shown in Figure 4.2 and they exhibit similar characteristics. After compression, peaks were smoothed and grouped. If the angular relationship of the strongest peaks among three pole figures is considered before and after compression, it appears that a preexisting <110> fiber texture in the normal direction is strengthened by deformation. The (111) poles observed in the range of  $\Theta = 30 \sim 40^{\circ}$  and the (200) poles in the range of  $\Theta =$ 40~50° are consistent with <110> fiber texture, and the same grains contribute to the higher intensities in all 3 pole figures. After compression, most of the grains contributing

to the <110> texture were not moved from their original orientation. Instead of rotation, these zones accumulated more grains in these orientations, so apparently the neighbor grains rotated to the preferred directions pre-existing before deformation. Qualitatively, similar texture changes occurred on both the inside and outside specimens. However, the changes in maximum intensity were opposite in the two specimens. The outside specimen had a much stronger initial intensity that resulted from a larger grain size [80]. These increases in intensity in orientations contribute to the <110> fiber texture but in the {220} pole figure, these orientations are near but not at the {220} pole.

#### 4.2.2. Texture at 650°C and 850°C

Figure 4.4 (a) shows the (111) pole figures before and after compression at  $650^{\circ}$ C. The initial texture also exhibits an apparently random distribution of high intensity poles but the deformed one indicates that several clusters are formed around at  $\Theta = 30 \sim 40^{\circ}$ . The (200) pole and (220) pole figures are shown in Fig. 4.5 (a) and 4.6 (a). The (220) strong texture component exists not at the center but near the center. In every pole figure, the maximum intensity has decreased, so deformation caused a spreading of crystal orientations.

Figure 4.4 (b) shows the (111) pole figures after compression at  $850^{\circ}$ C. The texture observed is similar to the other undeformed outside specimens, but the deformed one shows the textured state. The clustering effect is also detected at  $850^{\circ}$ C as in the other specimens. The maximum intensity in each cluster is located around  $\Theta = 35^{\circ}$ , even

though the range of each cluster spreads out around the poles with the maximum intensities. Figure 4.5 (b) shows the (200) pole figure. The majority of the textured component appears to be situated around  $\Theta = 40 \sim 50^{\circ}$  in the deformed case. Figure 4.6 (b) shows the (220) pole figure. Unlike the other specimens, it is difficult to observe the formation of any strong textured component just by looking at the pole figures, even though the slight increase in texture component about  $\Theta = 0^{\circ}$  is barely observed. As with the 650°C specimen the maximum intensity tends to decrease, and this indicates a general spreading of crystal orientations.

Although all pole figures exhibit similar features, the undeformed specimen in the center of the cast rod in Figure 4.1 (a) has a weaker texture, that correlates with a smaller grain size [80].

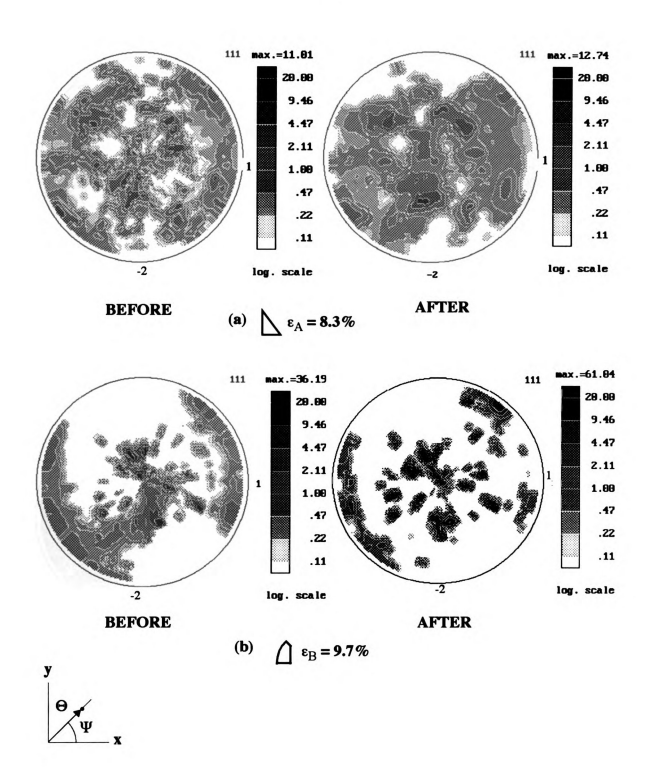


FIGURE 4.1 (111) Pole Figures before and after compression at room temperature in inside specimen (a)  $\,\epsilon=8.3\,\%$  and (b) outside specimen  $\epsilon=9.7\,\%$  .

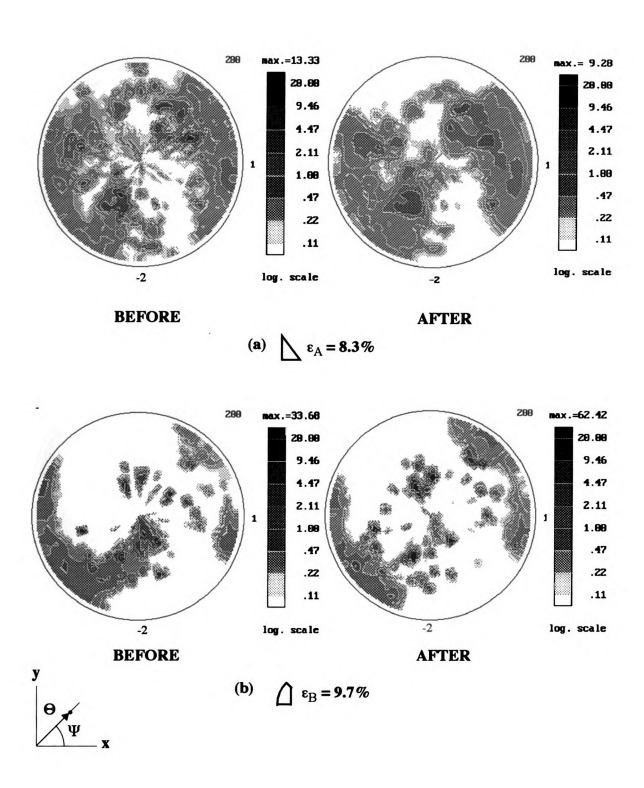


FIGURE 4. 2 (200) pole Figure before and after compression at room temperature in inside specimen (a)  $\epsilon$  = 8.3% and (b) outside specimen  $\epsilon$  = 9.7%

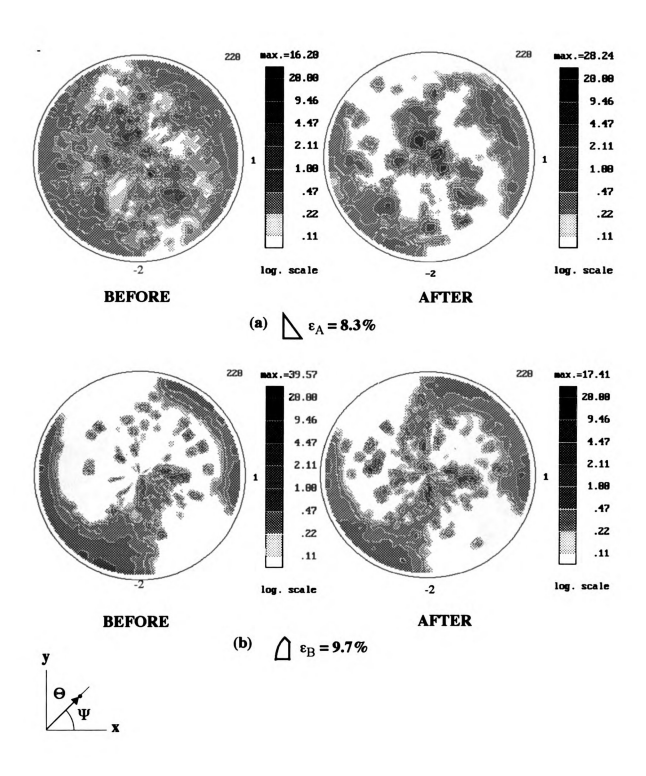


FIGURE 4. 3 (220) Pole Figures before and after compression at room temperature in inside specimen (a)  $\epsilon$  = 8.3% and (b) outside specimen  $\epsilon$  = 9.7%.

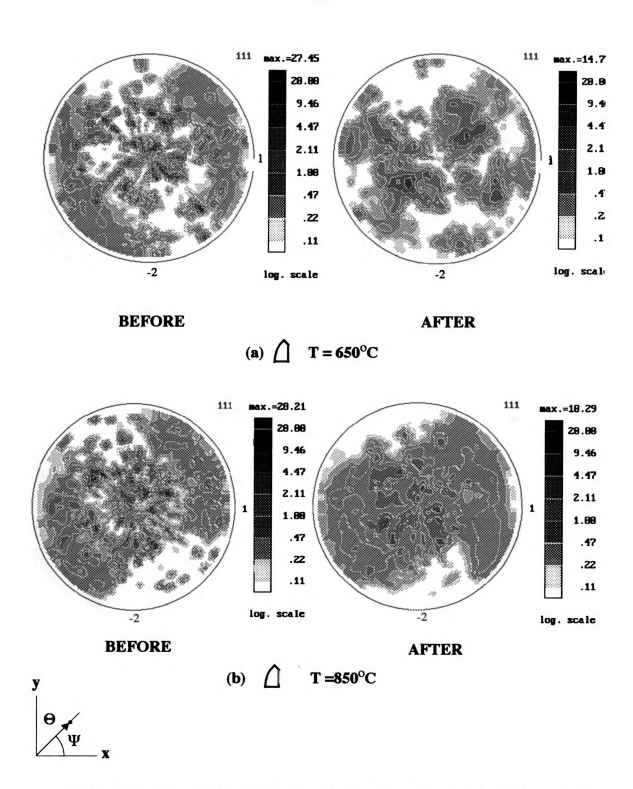


FIGURE 4. 4 (a) (111) pole figures before and after compression at 650°C,  $\epsilon$  = 8.2% (b) (111) pole figures before and after compression at 850°,  $\epsilon$  = 4.8%

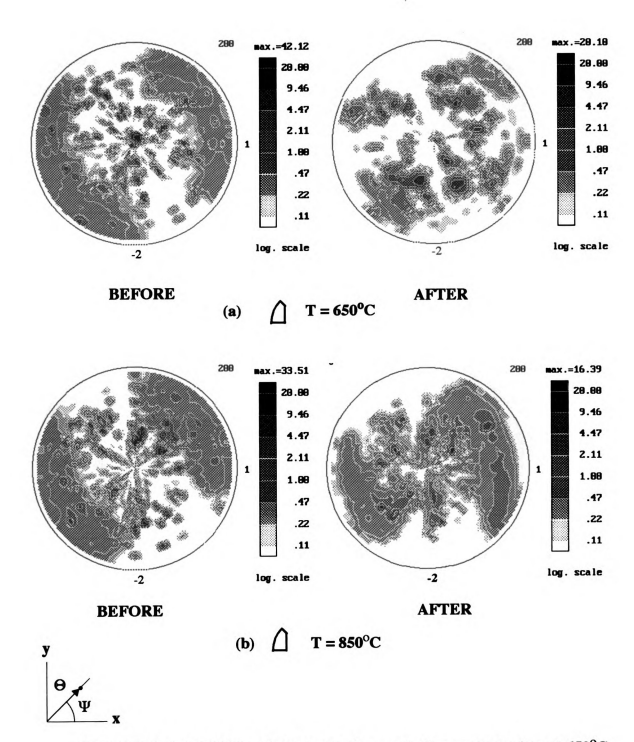


FIGURE 4. 5 (a) (200) pole figures before and after compression at 650°C,  $\epsilon$  = 8.2% and (b) at 850°C,  $\epsilon$  = 4.8%

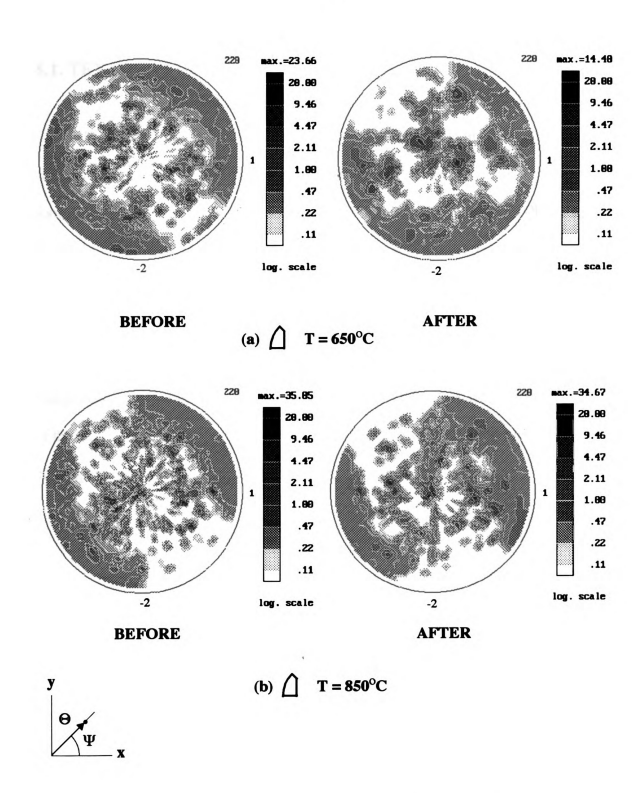


FIGURE 4. 6 (a) (220) pole figures before and after compression at 650°C,  $\epsilon$  = 8.2% and (b) at 850°C,  $\epsilon$  = 4.8%

# 5. ANALYSIS AND DISCUSSION

# **5.1. TEXTURE FORMATION**

Figures 5.1- 5.4 show the SOD's (Sample Orientation Distribution) after compression at room temperature,  $650^{\circ}$ C and  $850^{\circ}$ C. In homogeneous axisymmetric uniaxial deformation of a specimen with truly random grain orientations, SOD sections ( $\Psi$  = constant) should be all the same and identical to the projection, which represents the inverse pole figure in the axial direction. The SOD sections of the TiAl specimen indicate dependence upon  $\Psi$  which arises from the initially non random texture. The inverse pole figures after compression in Figure 5.5 show that the dominant final component is the <110> type fiber component in the normal direction in every specimen. With strain, the maximum intensity of the inverse pole figures increase dramatically, but the maximum intensities in the elevated temperature deformation decrease slightly.

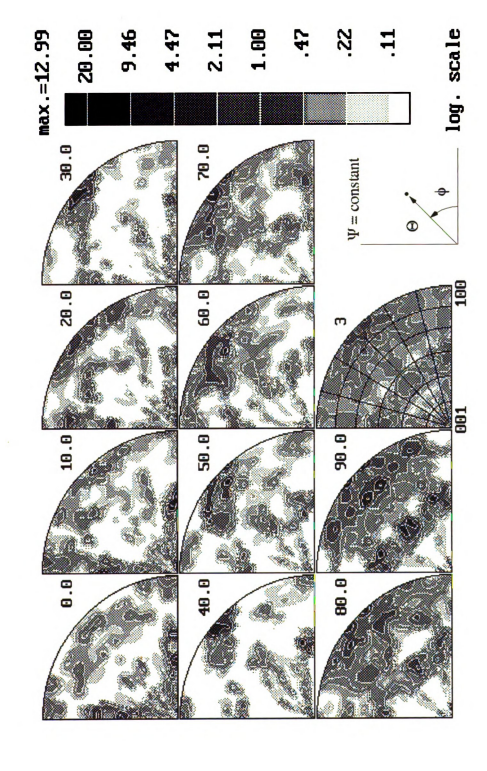


FIGURE 5.1 Complete SODF after compression at room temperature in inside specimen  $\sum \varepsilon = 8.3\%$ 

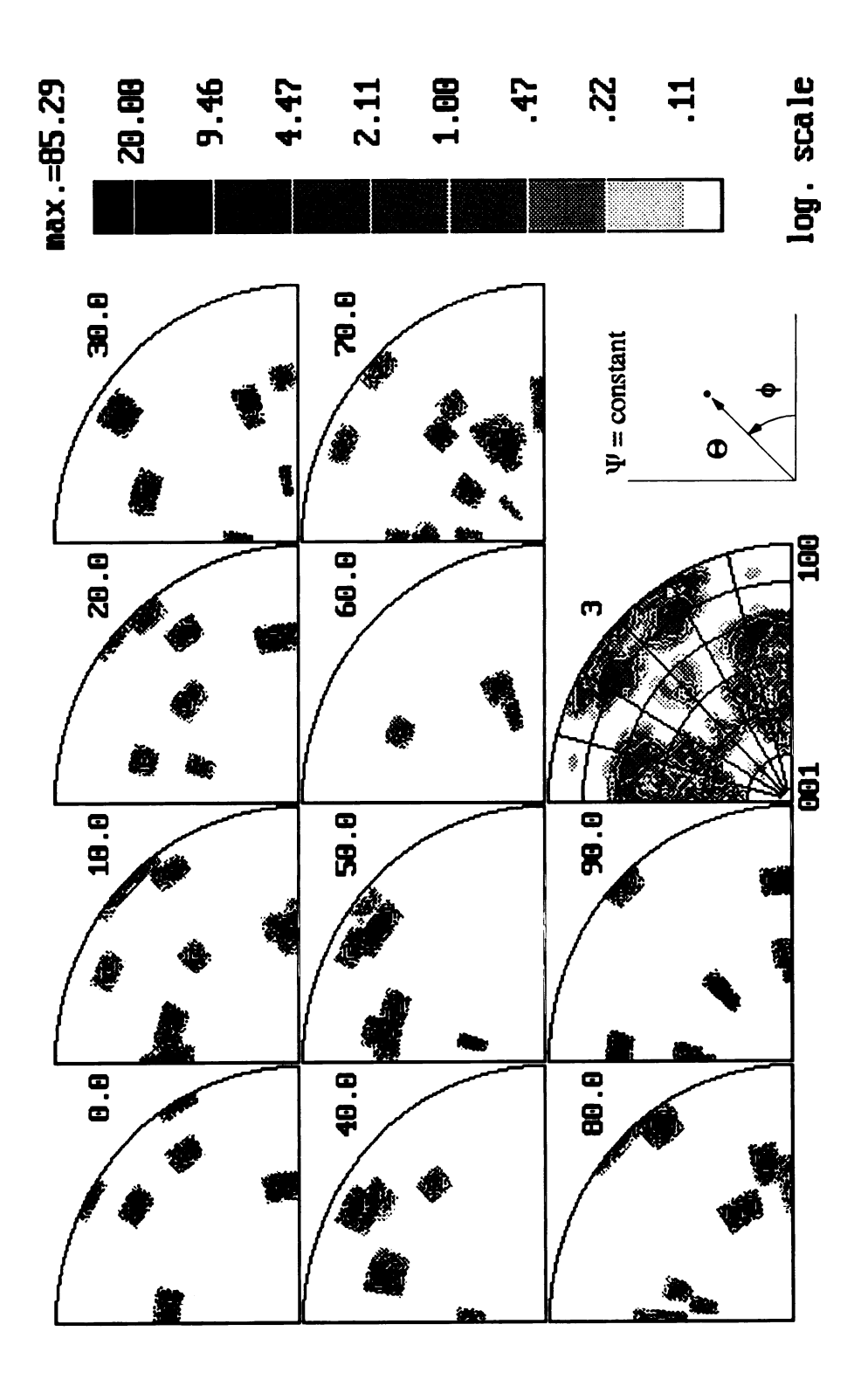


FIGURE 5.2 Complete SODF after compression at room temperature in outside specimen

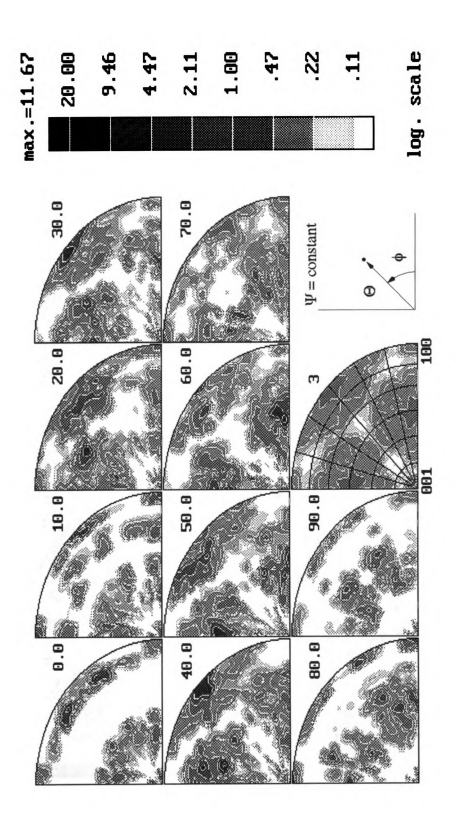


FIGURE 5.3 Complete SODF after compression at  $650^{\circ}\mathrm{C}$  .

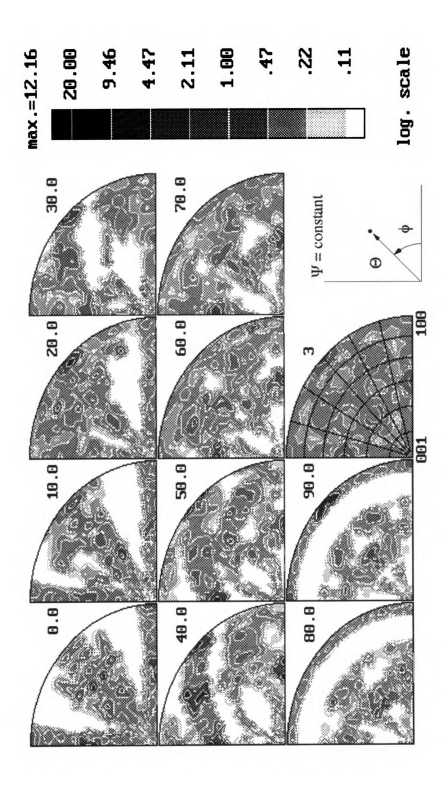


FIGURE 5.4 Complete SODF after compression at 850°C  $\int$  c = 0

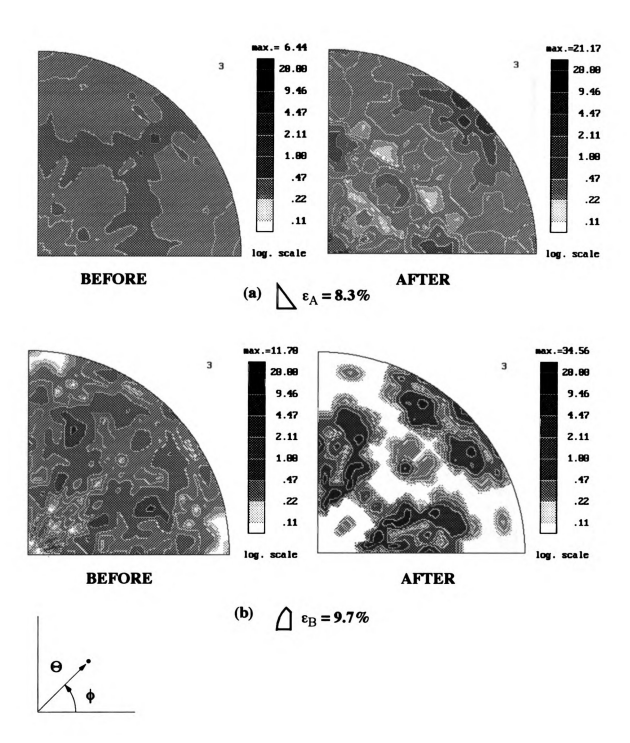


FIGURE 5. 5 Inverse pole figures at normal direction before and after compression at room temperature in inside specimen (a) and outside specimen (b).

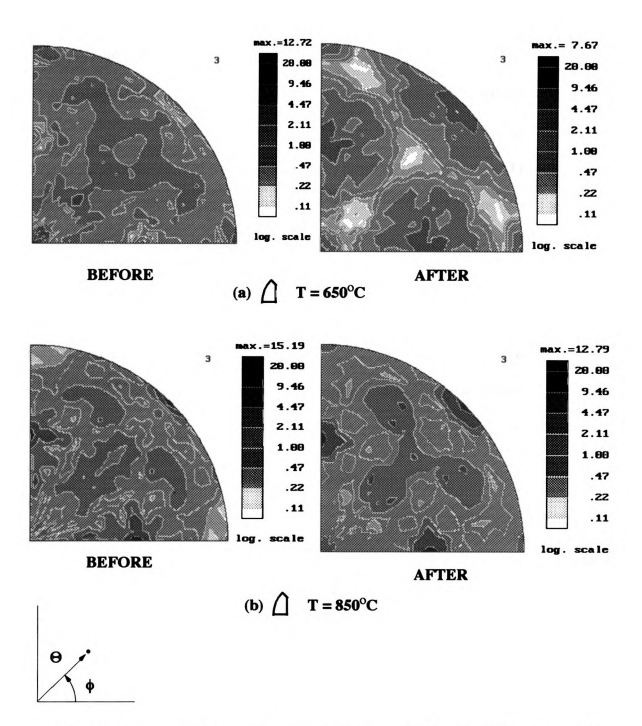


FIGURE 5. 6 Inverse pole figures before and after compression (a) at 650°C,  $\,\epsilon$  = 8.2% and (b) at 850°C,  $\,\epsilon$  = 4.8%

## **5.2.THE PREDICTION OF TWINNING**

#### 5.2.1. Schmid Law

One of purposes in this research is to examine the possibility of detecting mechanical twinning by analysis of texture changes. For this purpose, the Schmid factor for twinning in TiAl was calculated and represented on a stereographic projection. For tension and compression, different stress geometries are required. In Figure 5.7, assuming the bottom of the specimen is fixed, the twinning critical resolved shear stress must have a component parallel to the principle stress direction. Since twinning only occurs in one direction, the same twinning system must be rotated 90° from tension geometry to compression geometry. Figure 5.8 shows the comparison of the Schmid factor contours between tension and compression. For the case of tension, the maximum Schmid factor is positioned in the vicinity of  $[44\overline{1}]$  crystal direction for the  $(111)[11\overline{2}]$  true twinning system [39]. The maximum Schmid factor for compression is located in the vicinity of [118] for the (111)[112] true twinning system. The stress axis which produces the highest Schmid factor for twinning in compression is close to a [001] cube orientation, while in tension, the stress axis is near the [110] orientation.

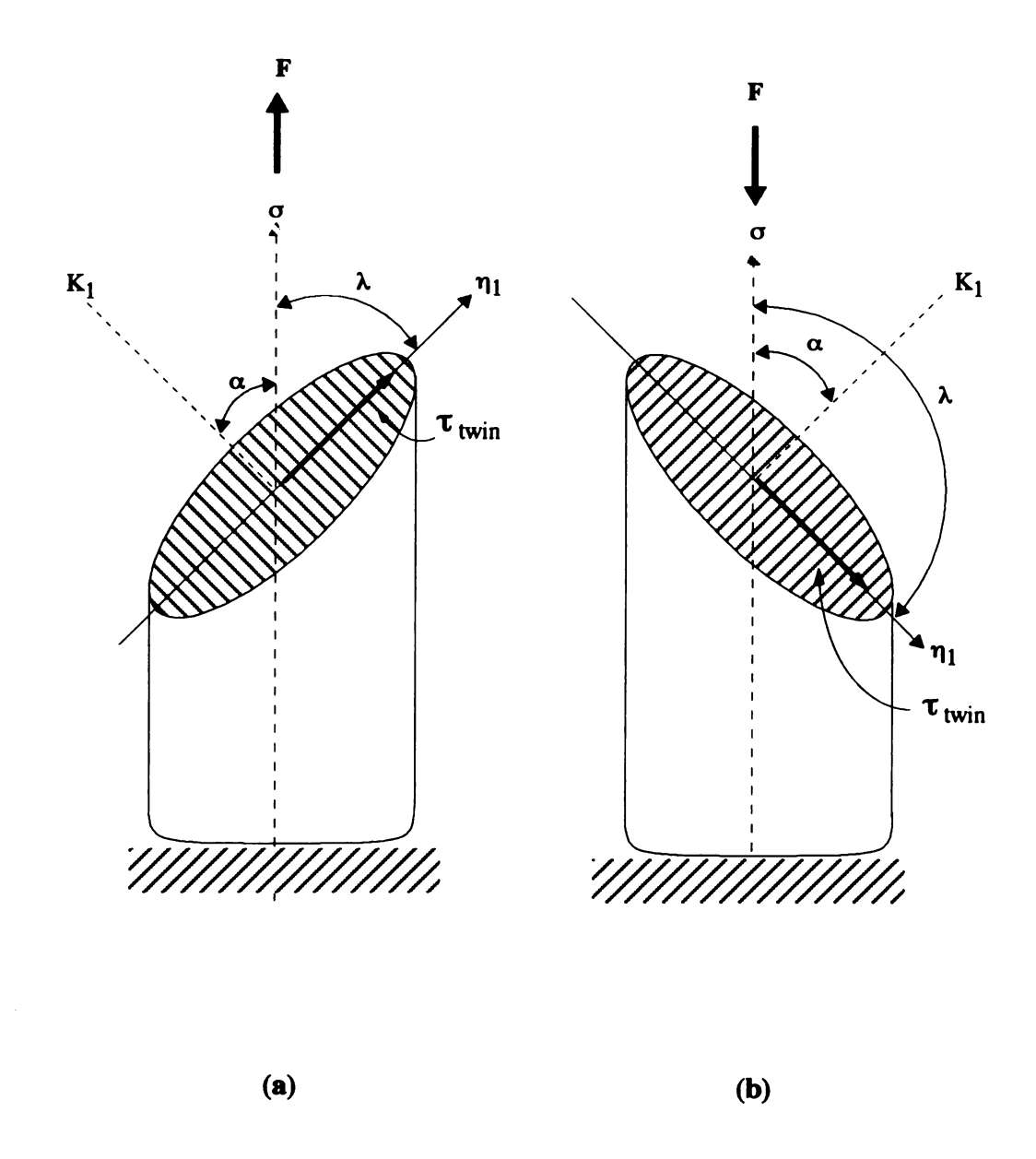


FIGURE 5. 7 (a) Tension (b) Compression, Slip plane normal  $K_1$  , slip direction  $\eta_1$  , stress axis  $\sigma$  , and loading direction F.

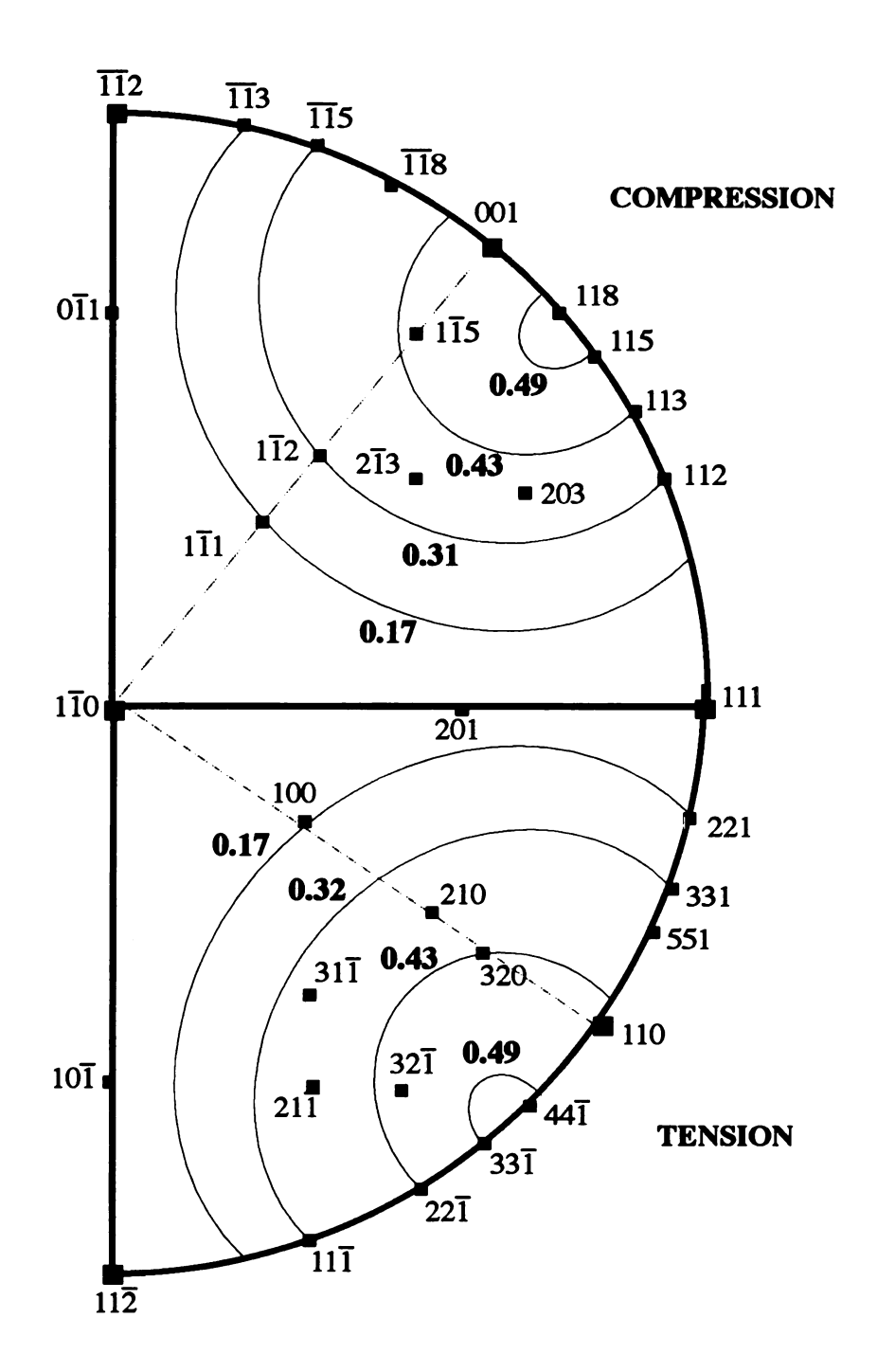


FIGURE 5.8 Estimated Schmid factor contours with respect to the true twinning system of (111)[112] which indicates that the highest Schmid factor is in the vicinity of [441] tensile principal stress axis [39] but in the vicinity of [118] for compression.

## 5.2.2. Detection of Mechanical Twinning

For detecting a change of texture due to the mechanical twinning, two theoretical approaches are used. The first can be called a pre-deformation approach and the second one can be called a post-deformation approach. The first case is related to the crystallographic approach for twinning. Basically, it assumes that the initial distribution of grains before deformation is random. With this initial condition, as the stress is imposed in the compressive direction, the randomly oriented grains start to rotate, according to the orientation of each crystal with respect to the local stress state during deformation. For mechanical twinning, the stress condition is estimated with the Schmid law. Generally, crystallographic twinning is described by one of two possible rotation axes. The true twinning system in TiAl is described by the normal direction of the (111) plane and the [112] slip direction which are identified as the  $K_1$  plane normal and the  $\eta_1$  slip direction, respectively, in the crystallographic description of twinning. These directions are shown in Figure 5.7. If a grain is rotated about 180° around either of these two rotation axes for twinning, it will arrive at the final twinning orientation after deformation. The (111) pole figure will give an appropriate way to illustrate the detection of the orientation change of each grain. In Figure 5.9, a grain is oriented in a way so that the normal direction coincides with the principal stress axis that provides the highest Schmid factor for true twinning in the initial condition (Figure 5.9 (a)). The twinning deformation resulting from loading in the normal direction will rotate the grain around the (111) rotation axis and the grain will reach the twinned orientation in Figure 5.9 (b).

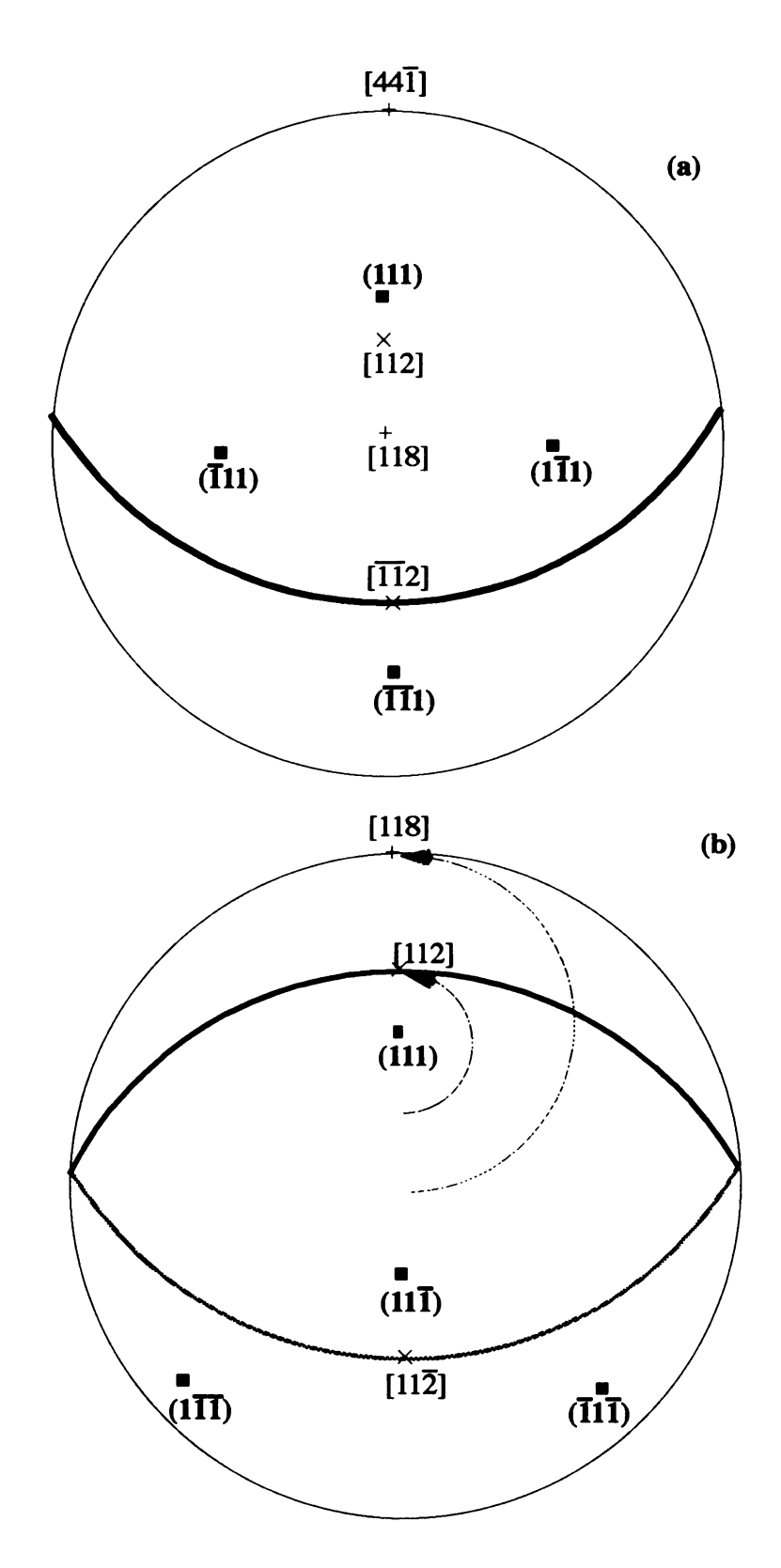


FIGURE 5. 9 (111) Pole Figures before (a) and after true twinning (b) illustrate how texture changes.

However, this approach has theoretical and experimental inaccuracy. In polycrystal deformation, grains do not rotate just following the Schmid law but deformation must satisfy much more complicated polycrystalline plasticity theories. Therefore, the initial assumption that only used the Schmid law is oversimplified in the theoretical view. Also, the clustering effect in the pole figures in Figures 4.1~6 is the dominant phenomena after deformation, which makes it difficult to identify a specific grain orientation.

Compared with this first approach, the post-deformation approach presents a more practical approach. The fundamental idea of the post deformation approach is to compare a component of texture in the initial condition before compression with the texture change after compression. For this, an inverse pole figure is employed as a tool for detecting the texture evolution, because it shows the general texture change at a glance. Figures 5.5-6 show inverse pole figures in four testing conditions which are recalculated from the ODF. The texture change before and after deformation, can be viewed by the difference between the pole figures. Figures 5.10~13 illustrate the orientations that were weakened, and the orientations that were strengthened. From initial orientations, the region near the <110> component is always stronger after deformation. Figures 5.11~12 show a comparison of orientations along the bottom of the inverse pole figures in Figures 5.5~6. There also exist several weakened portions in each inverse pole figure as illustrated in Figures 5.13~15. Then a deterministic relationship is considered between the weakened and the strengthened components shown in each inverse pole figure. In order to evaluate potential relationships, the Schmid factors for each possible deformation system are calculated. Table 5.1 shows the Schmid factors of slip systems, primary  $(111)[11\overline{2}]$  true twinning system and other

possible true twinning systems for several stress axis orientations in the 001-110-010 unit triangle (Figure 5.10). It should be noted that twinning shear is unidirectional, unlike slip. The region shaded in gray represents the stress axis orientations which have high Schmid factors for primary twinning and superdislocation slip.

From experimental observations, there is strengthening of the <110> fiber component, but also two weakened regions are observed at orientations of [212] and [328] directions respectively in Figure 5.13. For example, the [212] orientation has a Schmid factor for (111)<110> dislocation slip that is higher than the primary (111)[11\overline{2}] true twinning system. But for the [328] orientation, the Schmid factor for the primary true twinning system and superdislocation slip have a high values of Schmid factors. If superdislocation slip accounted for the deformation, then one would expect rotation of less than 4° for a strain of ~10%. So, it is likely that the grains oriented to [328] were mechanically twinned after the deformation at room temperature, if the critical resolved shear stress for twinning is similar or smaller than superdislocation. Similar considerations permit a comparison for superdislocation and normal slip that is also illustrated on Figure 5.10.

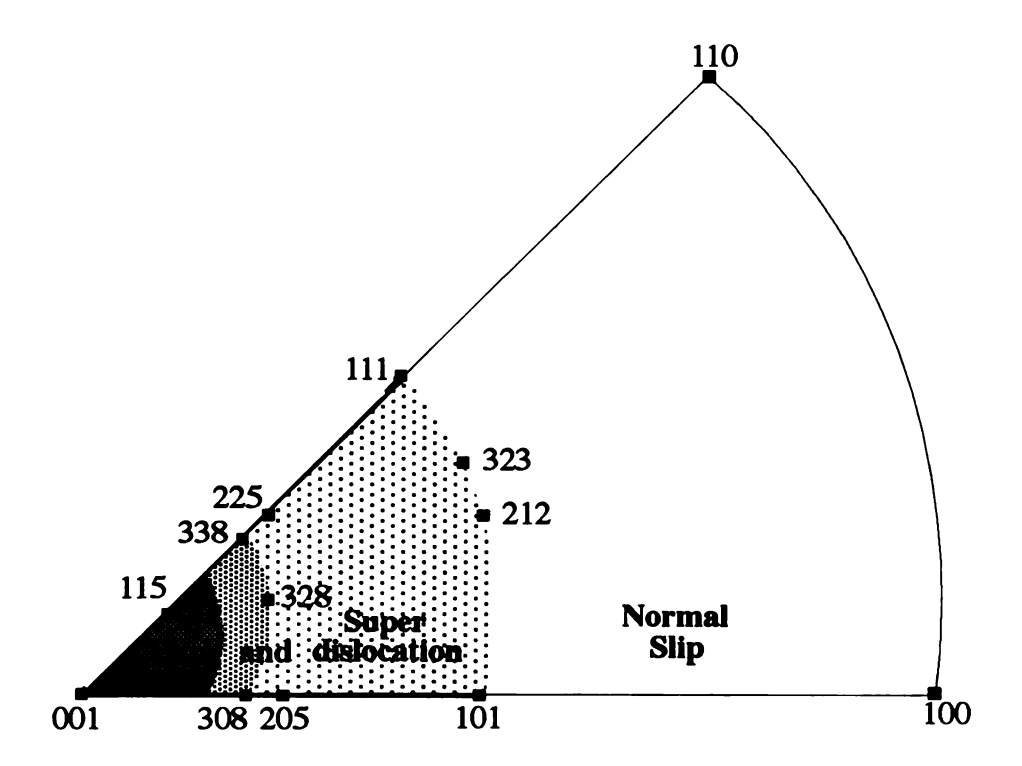


FIGURE 5. 10 Several stress axis orientations in 001 101 111 unit triangle.

Table 5.1 Schmid factors of several deformation systems according to stress axis orientations

		100	115	338	328	308	205	225	323	212
	(111)[110]	0	-0.1512	-0.2390	-0.2386	-0.1846	-0.1971	-0.2474	-0.3711	-0.4082
Slip	(111)(101]	-0.4082	-0.3024	-0.1991	-0.2386	-0.3076	-0.3064	-0.1856	0	0
	(111)[011]	-0.4082	-0.4536	-0.4381	-0.4772	-0.4921	-0.4023	-0.4330	-0.3711	-0.4082
Primary Twinning	[111][111 <u>7]</u>	-0.4717	-0.4889	-0.4024	-0.4377	-0.4617	-0.4551	-0.3867	-0.0086	-0.1309
Possible	$(\overline{11})[\overline{12}]$	-0.4717	-0.4372	-0.3734	-0.4132	-0.4622	-0.4551	-0.1789	-0.2568	-0.0791
True	(T11)(T12]	-0.4717	-0.4372	-0.3681	-0.3642	-0.3071	-0.2930	-0.3572	-0.1500	-0.1311
Twinning	(III)[II2]	-0.4717	-0.3140	-0.1271	-0.1931	-0.3071	-0.2930	-0.1362	0.2791	0.1831
Slip in	(111)( <u>1</u> 10)	0	0	0	-0.0689	-0.1846	-0.1971	0	-0.1485	-0.2268
(111) plane	(111)[101]]	-0.4082	-0.4234	-0.3340	-0.3446	-0.3119	-0.2956	-0.3340	0	0
	(111)[01]]	-0.4082	-0.3024	-0.1991	-0.4136	-0.4921	-0.4927	-0.1856	-0.1485	-0.2268

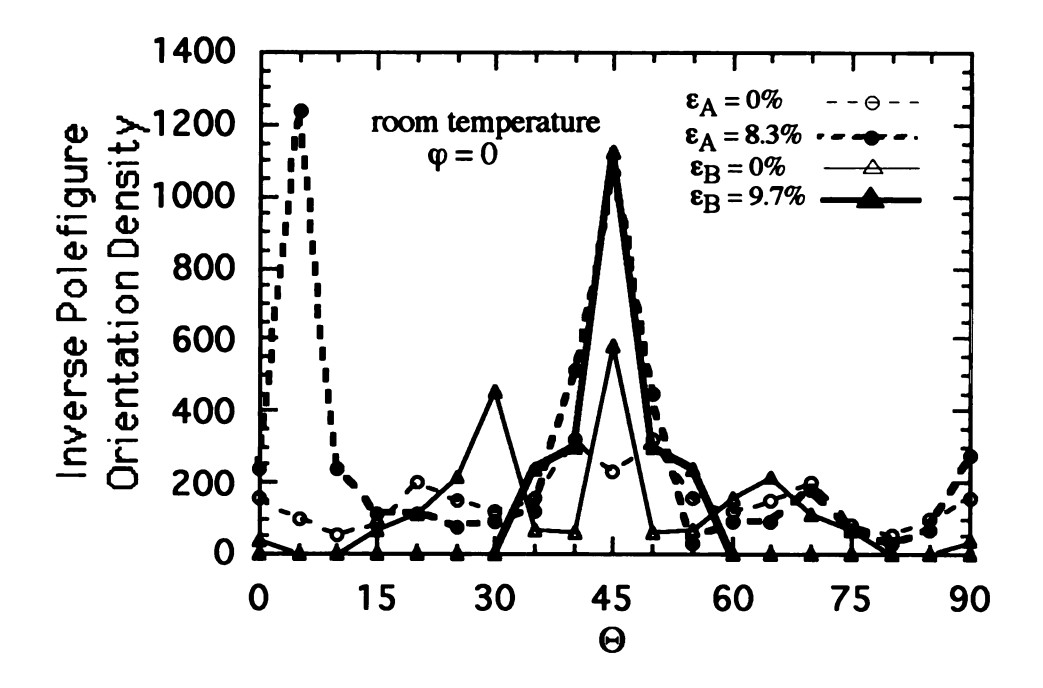


FIGURE 5. 11 (110) component density diagram according to change of  $\Theta$  at  $\phi=0$  before compression and after compression at room temperature in specimen (A)  $\epsilon=0\%$  and  $\epsilon=8.3\%$ , and (B)  $\epsilon=0\%$  and  $\epsilon=9.7\%$ .

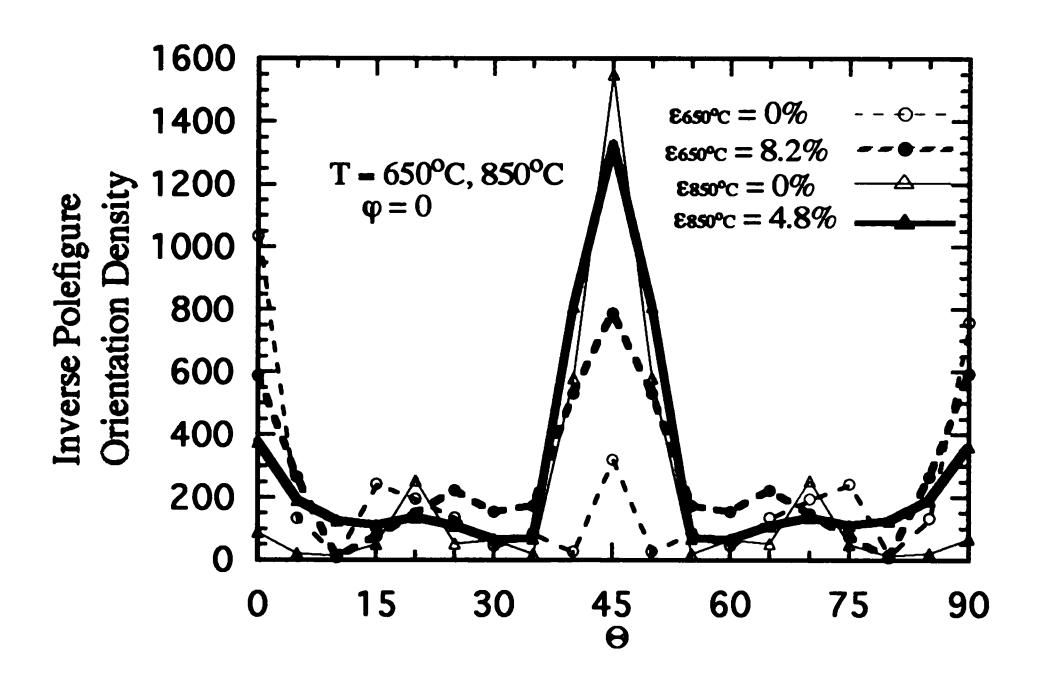


FIGURE 5. 12 (110) component density diagram according to change of  $\Theta$  at  $\Psi=0$  before compression and after compression at 650°C in  $\epsilon=0$  and  $\epsilon=8.2\%$ , and at 850°C in  $\epsilon=0$  and  $\epsilon=4.8\%$ 

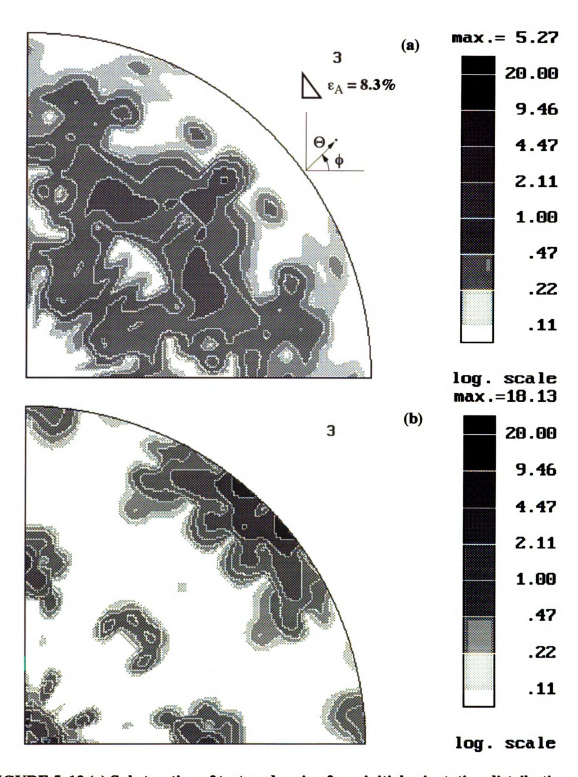


FIGURE 5. 13 (a) Substraction of textured region from initial orientation distribution (b) Substraction of initial orientation distribution from textured state at room temperature experiment for normal direction in inverse pole figure in inside specimen

 $\epsilon_A = 8.3\%$ 

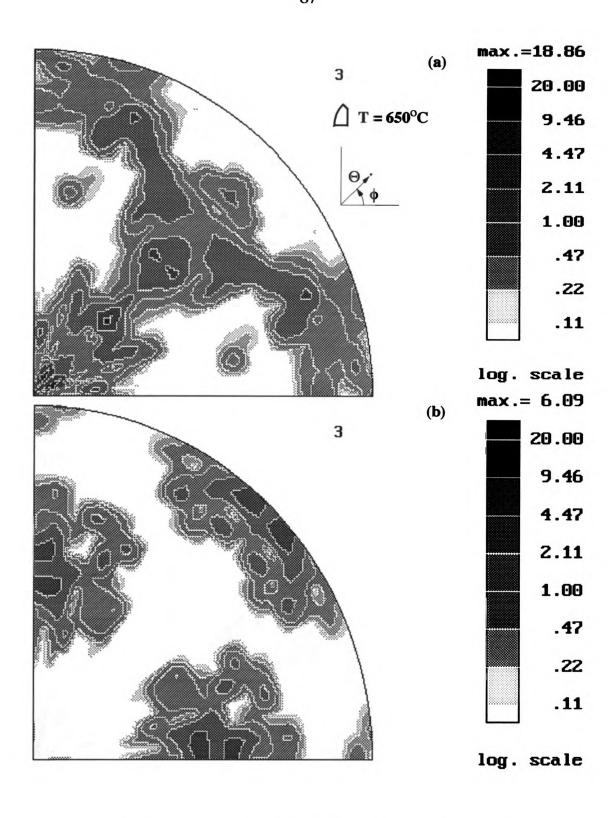


FIGURE 5. 14 (a) Substraction of textured region from initial orientation distribution (b) Substraction of initial orientation distribution from textured state at  $650^{\circ}$ C experiment for normal direction in inverse pole figure

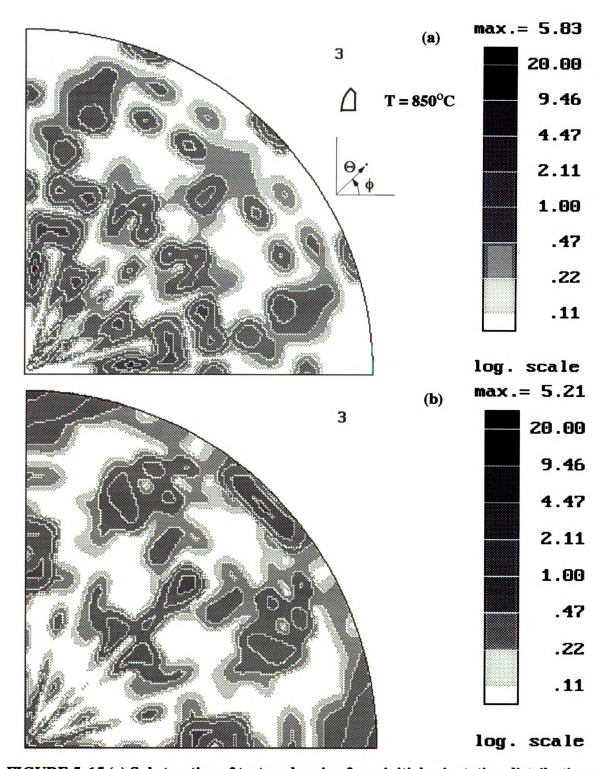


FIGURE 5. 15 (a) Substraction of textured region from initial orientation distribution (b) Substraction of initial orientation distribution from textured state at  $850^{\circ}$ C experiment for normal direction in inverse pole figure

At this point, the pre-deformation approach is employed as a verification tool for this result. Once the origin of the twinned area is identified as [328], it is assumed that (328)[21 $\overline{1}$ ] is the original texture component ([21 $\overline{1}$ ] is chosen arbitrarily in rolling direction). This component is rotated about  $180^{\circ}$  around the (111) pole or the [11 $\overline{2}$ ] direction. The resultant component after this rotation is (891)[ $\overline{1}1\overline{1}$ ] where the [ $\overline{1}1\overline{1}$ ] is in the resulting in -plane direction. The Euler angles of this component are shown in Table 5.2. Figure 5.16 shows the SOD sections after deformation which correspond to each Euler angle at room temperature. As shown in Figure 5.16, it appears that the twinning component is detected in each SOD section. Similar exercises with different choices of the in-plane direction resulted in similar values of  $\Theta$  and  $\phi$ , but  $\Psi$  varies with the choice of the in-plane direction. However, since the inverse pole figure is the summation of the  $\Psi$  sections of the SOD, it can be shown that any in-plane direction will lead to a twinned orientation near to 110 or 101.

Figures 5.6 (a) and 5.14 show the inverse pole figure and the difference pole figures for the compression at 650°C. Here, the most weakened area is detected near in the [115] direction. The Schmid factor for this direction has larger value for the true twinning system than those for other deformation systems. If the initial component for the twinning is (115)[110], the twinning component becomes (12121)[110]. The Euler angles for the twinning component are also shown in the table 2. Figure 5.17 shows the SOD section for these Euler angles. The twinning component is shown in the SOD. Figures 5.6 (b) and 5.15 show the inverse pole figure and the difference pole figures for the deformation at 850°C. It appears that [328] is also a twinned position similar to the room temperature experiment.

But, the amount of weakening is less than the case at room temperature. The Euler angles and SOD sections are shown in Figure 5.18.

	Ψ,	θ,	ф	Ψ,	Θ,	ф	Ψ,	Θ,	ф
(891)[111]	30,	42,	82	39,	48,	6	54,	85,	41
$(\overline{1212}1)[\overline{1}10]$	3,	45,	4	90,	86,	45			

Table 5.2 Euler angles for twinned components

These particular examples suggest that the orientation change in the range of  $0 < \Theta$   $< 25^{\circ}$  occurred by twinning. As shown in the literature survey, deformation due to slip causes gradual changes in texture such that after 40% rolling, the strength of the texture is only about 6 x random, but in TiAl, 5-9% compression can causes much greater increases in the texture strength. In conventional metals, twinning occurs after much slip hardening has occurred, but in TiAl it appears that twinning occurs with very early strains. A similar trend was also shown in the outside specimen at room temperature.

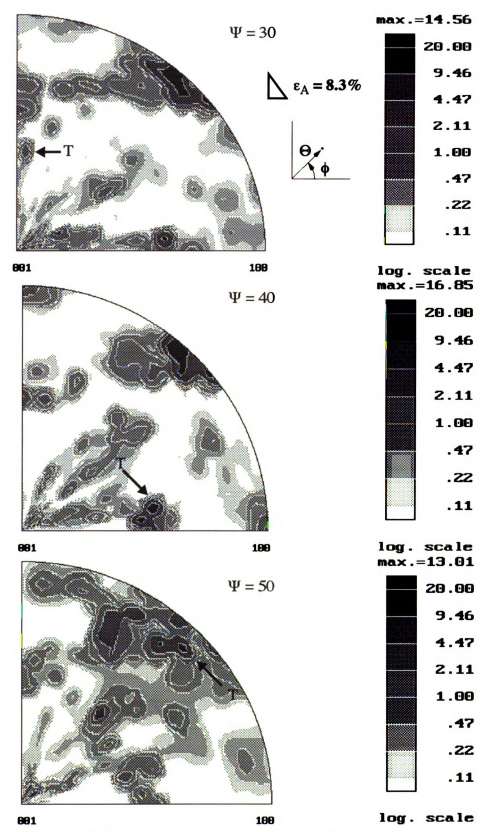


FIGURE 5. 16 SOD sections which include twinning component after deformation at room temperature in inside specimen (A) (T = Twin component).

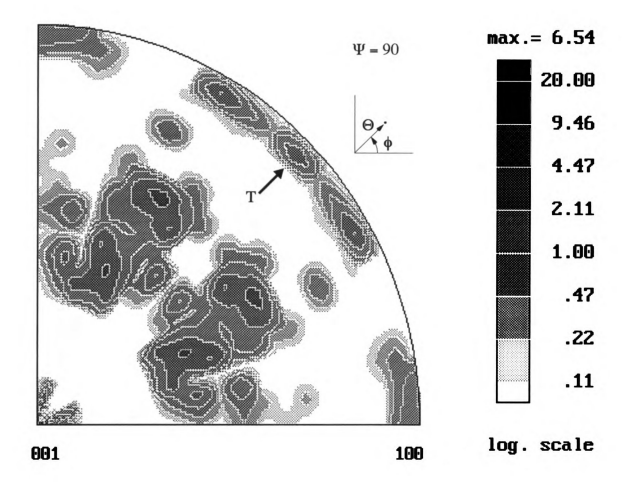


FIGURE 5. 17 SOD sections which include twinning component after deformation at 650°C (T = Twin component)

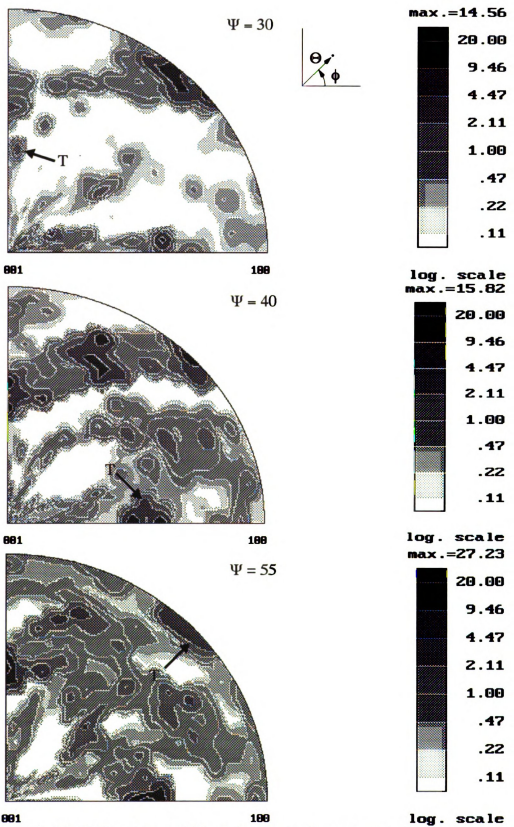


FIGURE 5. 18 SOD sections which include twinning component after deformation at 850°C (T = Twin component)

## 5.2.3. Volume Fraction of Twinning

Up to this point, the analysis of the mechanical twinning has been the major focus, which can be demonstrated in a qualitative matter. Next, a quantitative approach is used to determine the volume fraction V<sub>f</sub> of twinning. The volume fraction of twinning is calculated in the following procedure

$$V_f = \frac{\sum A_{twin}MWB}{\sum A_{total}MWT} - \frac{\sum A_{twin}MWA}{\sum A_{total}MWT}$$
 EQ. 5.1

Volume Fraction of Twinning

V<sub>f</sub> A<sub>twin</sub> = Twinned Area = Total Area

Mean Weight of Twinned Area Before Compression Mean Weight of Twinned Area After Compression
 Mean Weight of Total Area

Table 5.3 Data of strain due to mechanical twinning.

Temperature	Shape	ε <sub>total</sub> (%)	V <sub>f</sub> of twinning (%), range of Θ	ε <sub>total</sub> due to twin- ning (%)	fraction of total $\varepsilon$ due to twinning (%)
room temp.	7	8.3	2.05, 10~20°	1.45	17.5
room temp.	Δ	9.7	2.17, 0~20°	1.53	15.7
650°C	Δ	8.2	5.90, 10~20°	4.17	50.8
850°C	Δ	4.8	2.39, 10~20°	1.69	35.2

The IPF data is stored as an array of data at  $5^{\circ}$  increments of  $\Theta$  and  $\phi$ . Since these data represent an orientation density at a position on the surface of a sphere, the area associated with each data point must be computed. The popLA was used that determines the area bounded by  $5^{\circ}$  data points on the surface of a sphere, and averages the density values D  $(\Theta, \phi)$  on the corners of the area linearly.

In EQ. 5.1, the twinned area indicates the region with a weakened intensity where has higher Schmid factors for the primary twinning than those for other deformation systems (Figure 5.10). By applying this equation to the inverse pole figures of the inside specimen at room temperature, 650°C and 850°C in Figure 5.5~6, the volume fraction transfer by twinning at each temperature were about 20% at 22°C, 50% at 650°C and 35% at 850°C. The interesting point is that at 850°C, the volume fraction dropped by a large amount. This result is consistent with Loiseau's and Jin's studies [39, 81]. Their suggestion is that there may be a transition temperature which determines the activity of the mechanical twinning. Actually, at the highest temperature, dislocations become more mobile due to the thermal activation, and some cube <100> dislocations become mobile, and mechanical twinning is relatively less favorable than dislocation motion. This lower amount may be a result of the initially strong [110] component. Further if it is assumed that the majority of the deformation occurred on the primary lip or twinning system, then the amount of strain caused by mechanical twinning can be estimated by multiplying the volume fraction by the FCC twinning shear strain of 0.707. These computations indicate that at 650°C, most of the deformation occurred by twinning, and less fractions twinned at room temperature and at 850°C in Table 5.3. This result suggests that the texture analysis can detect mechanical twinning quantitatively. More theoretical approach using texture simulation should be used in future work, to determine if the starting texture in these experiments will generate the deformed textures experimentally measured, if mechanical twinning has a low critical resolved shear stress.

## **5.3.MAIN COMPONENT OF TEXTURE.**

As shown in section 5.2.2, pole densities are high at about <110> direction in the three inverse pole figures. The main component of texture in uniaxial compression has been identified as <110> fiber component in previous works [82,83] and the present result is consistent with the literature. In the present work, {220} pole figures taken at RT and  $650^{\circ}$  show a slight deviation of the main texture component from  $\Theta = 0^{\circ}$  even though the inverse pole figures show {110} fiber. The above analysis can explain that twinning account for this. The initial assumption in the ODF calculation was Cubic symmetry of TiAl, even though the actual symmetry is tetragonal. Thus, it seems that the ODF calculation could be improved by using the correct tetragonal symmetry conditions.

### **5.4.MECHANISM OF TEXTURE FORMATION.**

#### 5.4.1. Grain Rotation

Figures 4.1, 4.4 (a) and 4.4 (b) show (111) pole figures before and after compression at each testing temperature. For the three cases, the initial orientation shows a slightly textured state. The inverse pole figures of the three initial states indicates a weak {110} fiber component. Thus, it is assumed that these initial textures were formed during the casting

and heat treatment history of the specimen. Formation of a sharp deformation texture from a nearly random orientation after a small deformation implies that dramatic orientation changes occur by polycrystal plasticity that includes twinning. The sharpness of texture in the deformed specimen is related to the amount of grain rotation that occurred. If there is any specific orientation of existing grains before deformation and it is a stable orientation after deformation, the orientation is reinforced by the grains which continuously rotate toward the stable orientation, as the deformation proceeds. In present works, the stable orientation is <110> in both cases before and after compression. This is consistent with the classical FCC compression case. The effect of twinning is that orientations far from 110 are discontinuously rotated to orientations near 110 which can then rotate with subsequent strain toward the <110> terminal orientation.

#### 5.4.2. Slip

The difference between TiAl and classical FCC deformation textures depends upon the anisotropic characteristic of TiAl which results in the constraints on each deformation mechanism. The first trial in this experiment to analyze the quantitative differentiation of the 022 reflection from the 220 reflection was not successful due to the limited resolution of the X-ray system. Theoretical simulation considering polycrystal plasticity has been done by Hartig et al. [84]. The results indicate that the final texture component depends on the value of the CRSS (Critical Reserved Shear Stress) of each deformation mechanism. If the CRSS value of slip on {111}<110> is larger than slip on {111}<101>, the final texture component is shifted to <110> fiber type and if the CRSS value is reversed, the resultant texture component is close to <101>. This indicates that the prevailing deformation mode

determines how the final texture component develops. In the present work, this distinction cannot be made.

#### **5.4.3. Mechanical Twinning**

Since the {111}<112> type mechanical twinning is a crucial deformation mechanism in the plasticity of TiAl, its role in the texture formation is expected to be important. The activation of sessile 1/6<112> partial dislocation which becomes mobile in the elevated temperature is believed to help the generation of the twinning. As discussed in section 5.2.2, mechanical twinning was detected at room temperature as well as at the elevated temperature and even more, the twinning component appears to contribute to the <110> fiber component. Thus, the mechanical twinning is clearly to be a significant deformation mechanism regardless of the testing temperature. Furthermore, the fact that the region near <110> becomes very strong with rather low strains due to mechanical twinning indicates that the CRSS for twinning is probably lower that for superdislocation slip.

#### 5.4.4. Dynamic Recrystallization

Recent research has shown that dynamic recrystallization occurs during high temperature deformation [85,86]. The reason why high temperature deformation involves recrystallization originates from the accumulation of deformation energy and the release through nucleation and growth of the recrystallized grains. With increasing temperature, There is a greater driving force for dynamic recrystallization. It is reported that in the texture formation of TiAl during high temperature compression, the dynamic recrystallization effect causes shifting of the pure <011> fiber deformation texture component to <032>

which is located between <011> and <010>. Thus, the transition from deformation texture to recrystallization texture occurs in the process of the competition between these two stable components during high temperature deformation. In the present work, the high temperature compression was performed at 850°C. The results of pole figures and ODF calculation indicate no detectable formation of this recrystallization component. For this result, two explanation can exist. First, Lee and his coworkers found that the BDTT (Brittle-Ductile Transition Temperature), about 800°C, is the initiation temperature of recrystallization in tension and compression and no evidence has been shown for dynamic recrystallization at lower temperatures [85]. Second, the strain is probably too low for dynamic recrystallization in this present work. At the BDTT, only the necking region, which is a highly stress concentrated region during deformation has shown dynamic recrystallization in tension. In this regard, dynamic recrystallization seems to occur in higher temperature and higher strain than this present work. Even if recrystallization occurred at the transition interval at low strain, the recrystallization region would be limited only to stress concentration region such as grain triple junctions or grain boundaries and the recrystallized grains would be so small compared with most of original grains which contribute to texture formation that they would be hard to be detected in the final texture.

#### 5.4.5. Crack formation and deformation of TiAl

The stress-strain curve at room temperature showed a deviation from those at higher temperatures especially in the elastic region. The final microstructure showed many cracks in the present specimen [79]. At low temperature deformation of TiAl, the poor mobility of slip systems causes the localization of stress, which is directly related to the initiation of

a crack. Thus, even if the applied stress reached the CRSS (Critical Reserved Shear Stress) for the 5 preferred slip and twinning systems, the localized stress condition would nucleate a crack ahead of starting plastic deformation. However, the curve at 650°C showed a consistency with one at 850°C in elastic region, so, it suggests that increasing temperature might release the localized stress condition by thermal activation. However, the question is which temperature would be the turning point from fracture dominant circumstance to a deformation dominant one. At this moment, this question remains for further investigation. As a result, it is assumed that the kinetics of the fracture nucleation mechanism and the deformation mechanism control the deformability of TiAl. Thus, the overall structure failure and plastic deformation occurs by a process of competition between crack nucleation and plastic deformation by slip and mechanical twinning.

# 6. CONCLUSION

- 1. The results of the texture analysis of TiAl in compression showed that the <110> fiber component is the dominant component through all testing temperatures in compression. The result is quite consistent with conventional FCC compression.
- Specimens taken from different parts of a cast and heat treated cylindrical rod have highly variable textures. They are stronger near the outside and weaker toward the center.
- 3. The present work indicated that the analysis of mechanical twinning in compression is possible through texture analysis. The present experiments indicate that mechanical twinning occurs at very low strains, and that it accounts for nearly all of the total strain at 650°C. At 850°C, where thermal activation makes all dislocation motion easier, the contribution of mechanical twinning is smaller. At room temperature, cracking complicates the interpretation, but mechanical twinning is clearly a significant contributor to the deformation.

# 7. REFERENCES

- [1]. M. Yamaguchi and Y. Umakoshi, Prog. Mater. Sci., 1990, Vol. 34, pp. 1-148
- [2]. E.S. Bumps, H.D. Kessler and M. Hansen, Journal of Metals, 1952, June, pp. 609-614.
- [3]. H.R. Ogden, D.J. Maykuth, W.L. Finlay and R.I. Jaffee, Journal of Metals, 1951, December, pp. 1150-1155.
- [4]. E. Ence and H. Margolin, Trans. AIME., 1961, vol. 221, pp. 151-157.
- [5]. S.C. Huang and P.A. Siemers, Metall. Trans., 1989, vol. 20A, pp. 1899-1906.
- [6]. C. McCullough, J.J. Valencia, H. Mateos, C.G. Levi, R. Mehrabian, Scripta Metall., 1988, vol. 22, pp. 1131-1136.
- [7]. C. McCullough, J.J. Valencia, C.G. Levi and R. Mehrabian, Acta Metall., 1989, vol. 37, No. 5, pp. 1321-1336.
- [8]. Y.W. Kim and D.M. Dimiduk, JOM, 1991, August, pp. 40-47
- [9]. H. A. Lipsitt, Mat. Res. Soc. Symp. Proc., 1985, vol. 39, pp. 351-364
- [10]. M. Takeyama, T. Kumagai, M. Nakamura and M. Kikuchi, The Minerals, Metals & Materials Society, 1993, pp. 167-176.
- [11]. G. Ramanath and Vijay K. Vasudevan, 1993, Mat.Res.Soc.Symp.Proc., Vol. 288, pp.

- 223-228
- [12]. P. Wang and V. K. Vasudevan, Mat.Res.Soc.Symp.Proc., Vol. 288, pp.229-236
- [13]. Y.W. Kim, Acta Metall., 1992, vol. 40, no. 6, pp. 1121-1134
- [14]. C.R. Feng, D.J. Michel and C.R. Crowe, Scripta Metall., 1988, vol. 22, pp. 1481-1486.
- [15]. C.R. Feng, D.J. Michel and C.R. Crowe, Scripta Metall., 1989, vol. 23, pp. 1135-1140.
- [16]. S.A. Jones, R.D. Shull, A.J. McAlister and M.J. Kaufman, Scripta Metall., 1988, Vol. 22, pp. 1235-1240
- [17]. D.S. Schwartz and S.M. L. Sastry, Scripta Metall., 1989, vol. 23, pp. 1621-1626.
- [18]. J.A. Graves, L.A. Bendersky, J.H. Perepezko and W.J. Boettinger, Mat. Sci. Eng., 1988, 98, pp. 265-268.
- [19]. Y.S. Yang and S.K. Wu, Scripta Metall., 1990, vol, 24, pp. 1801-1806.
- [20]. M. Yamaguchi, Mater. Sci. Tech., 1992, vol. 8, 229-307.
- [21]. S.C. Huang and E. L. Hall, Metall. Trans. A., 1991, Vol. 22A, pp. 427-439.
- [22]. J. Seeger, A. Bartels and H. Mecking, Scripta Metall., 1991, Vol. 25, pp. 2523-2528.
- [23]. J. Seeger and H. Mecking, Scripta Metall., 1993, Vol. 29, pp. 13-18.

- [24]. H.A. Lipsitt, D. Shechtman and R.E. Schafrik, Metall. Trans. A., 1991, Vol. 6A, pp. 1991-1996.
- [25]. S.C. Huang and E.L. Hall, Scripta Metall., 1991, Vol. 25, pp. 1805-1809
- [26]. P.P. Rao and K. Tangri, Mater. Sci. Eng., 1991, Vol 132, pp.49-59.
- [27]. S.H. Whang and Y.D. Hahn, Scripta Metall., 1990, Vol. 24, pp. 485-490.
- [28]. Y.W. Kim, JOM., 1989, July, pp. 24-29.
- [29]. Y.W. Kim and D.M. Dimiduk, Mat.Res.Soc.Symp.Proc., 1993, Vol. 288, pp.671-677.
- [30]. D.S. Shih, D.S. Schwarts and J.E. O'neal, Mat.Res.Soc.Symp.Proc., 1993, Vol. 288, pp. 579-584.
- [31]. V. Seethraman, S.L. Semiatin, C.M. Lombard and N.D. Frey, Mat.Res.Soc.Symp.Proc., 1993, Vol. 288, pp.513-518.
- [32]. O.A. Kaybyshev, G.A. Salishchev, R.M. Imayev and A.B. Notkin, Phys. Met. Metall., 1988, Vol. 65, No. 5, pp. 154-162.
- [33]. R.M. Imayev, O.A. Kaybyshev and G.A. Salishchev, Phys. Met. Metall., Vol. 71, No. 3, pp. 178-186.
- [34]. R.M. Imayev, O.A. Kaibyshev and G.A. Salishchev, Acta metall. Mater., 1992, Vol. 40, No. 3, pp.589-595.
- [35]. R.E. Reed-Hill, Physical Metallurgy Principles

- [36]. B.A. Bilby and A.G. Crocker, Proc. Roy. Soc. Lond. A, 1965, Vol. 288, pp.240-255.
- [37]. J.W. Christian and D.E. Laughlin, Acta metall., 1988, Vol. 36., No. 7, pp. 1617-1642.
- [38]. E. Goo, "Twinning in Advanced Materials", TMS, 1994, pp. 305-315.
- [39]. Z. Jin, "Mechanical Twinning in Creep Deformed in TiAl", 1993, Ph.D. Thesis.
- [40]. A. Couret, S. Farenc, D. Caillard and A. Coujou, "Twinning in Advanced Mtaetrials", TMS, 1994, pp. 361-374.
- [41]. D.S. Schwarts and S.M. Sastry, Scripta Metall. 1989, Vol. 23, pp. 1621-1626.
- [42]. George T. Gray III, "Twinning in Advanced Materials", TMS, 1994, pp. 337-349.
- [43]. S.F. Farenc, A. Coujou and A. Couret, Phil. Mag. A, 1993, Vol. 67, No. 1, pp. 127-142.
- [44]. D.Schechtman, M.J. Blackburn, and H.A. Lipsitt, Metall. Trans., 1974, Vol. 5, pp. 1373-1381.
- [45]. B.A. Greenberg and Yu. N. Gornostirev, Scripta Metall., 1988, Vol. 22, pp. 853-857.
- [46]. B.A. Greenberg, V.I. Anisimov and Yu.N. Gornostirev, Scripta Metall., 1988, Vol. 22, pp. 859-864.
- [47]. S.A. Court, J.P.A. Lofvander, M.A. Stucke, P. Kurath and H.L Fraser, Mat. Res. Soc. Symp. Proc., 1989, Vol. 133, pp. 675-680.

- [48]. S.A. Court, V.K. Vasudevan and H.L. Fraser, Phil. Mag. A, 1990, Vol. 61, No. 1, pp. 141-158.
- [49]. C. Woodward, J. Maclaren and S. Rao, J. Mater. Res., 1992, Vol. 7, No. 7, pp. 1735-1749
- [50]. S. Swaminathan, I.P. Jones, N.J. Zaluzec, D.M. Maher and H.L. Fraser, Mater. Sci. Egr., 1993, Vol. A170, pp. 227-235.
- [51]. T. Kawabata, M. Tadano and O. Izumi, 1988, Vol. 22, pp.1725-1736
- [52]. V.K. Vasudevan, S.A. Court, P. Kurath and H.L. Fraser, Scripta Metall., 1989, Vol. 23, pp. 907-912
- [53]. V.K. Vasuden, M.A. Stucke, S.A. Court and H.L. Fraser, Phil. Mag. Let., 1989, Vol.59, No. 6, pp. 299-307.
- [54]. S. Sriam, V.K. Vasudevan and D.M. Dimiduk, Mat. Res. Soc. Symp. Proc., 1991, Vol. 213, pp.375-383.
- [55]. E.L. Hall and S.C. Huang, Mat. Res. Soc. Symp. Proc., 1989, Vol. 133, pp. 693-698.
- [56]. H.J. Bunge, "Texture Analysis in Materials Science", Butterworths.
- [57]. U.F. Kocks, "A Symmetric Set of Euler Angles and Oblique Orientation Space Sections"
- [58]. "Standard Distributions in Texture Analysis", Akademie-Verlag Berlin, 1987.

- [59]. U.F. Kocks, Metall. Trans., 1970, Vol. 1, pp. 1121-1143.
- [60]. H. Mecking, "Strength of Metals & Alloys", Proceedings of the 5th International conference, 1979, Vol 3. pp. 1573-1594.
- [61]. D. Kuhlmann-Wilsdorf, Mat. Sci. Eng., 1989, Vol. A113, pp. 1-41.
- [62]. G.I. Taylor, J. Inst. Met., 1938, Vol. 62, pp. 307-24.
- [63]. J.F.W. Bishop and R. Hill, J. Mech. Phys. Solids, 1954, Vol. 3, pp. 130-142.
- [64]. J.D. Livingston and B. Chalmers, Acta Metall., 1957, Vol. 5, pp. 322-327.
- [65]. U.F. Kocks, Acta Metall., 1958, Vol. 6., pp. 85-94.
- [66]. U.F. Kocks, Acta Metall., 1960, Vol. 8, pp. 345-352.
- [67]. T.H. Lin and B. Lieb, J. Mech. Phys. Solids, 1962, Vol. 10. pp. 65-72.
- [68]. E.A. Calnan, Acta Metall., 1954, Vol. 2, pp. 865-874.
- [69]. U.F. Kocks, Acta Metall., 1966, Vol. 14, pp. 87-98.
- [70]. B. Ramaswami, U.F. Kocks and B. Chalmers, Trans. Metal. AIME., 1965, pp. 927-931.
- [71]. R.E. Smallman, J. Ins. Metal., 1955, Vol. 84, pp. 10-18.
- [72]. R.F. Braybrook and E.A. Calnan, J. Ins. Meta., 1956, Vol. 85, pp. 11-14.

- [73]. Y. Zhou, L.S. Toth and K.W. Neal, Acta Metall., 1992, Vol. 40, No. 11, pp. 3179-3193
- [74]. R.E. Smallman and D. Green, Acta Metall., 1964, Vol. 12, pp. 145-154
- [75]. I.L. Dillamore, J.G. Roberts, and A.C. Bush, Metal Sci., 1979, pp. 73-77
- [76]. J. Hirsch, K. Lucke and M. Hatherly, Acta Metall., 1988, Vol. 36, No. 11, pp. 2905-2927
- [77]. C.H. Wu, Master thesis, Michigan State University, 1995.
- [78]. M.F. Spotts, "Design of Machine Elements", Fourth edition, 1971.
- [79]. J.Sadowitz, Senior thesis, Dept. MSM, Michigan State Univerity, 1995.
- [80]. J.S. Kallend, U.F. Kocks, A.D. Rollett and H.-R Wenk, Mater. Sci. Eng., 1991, A132, pp. 1-11.
- [81]. A. Loiseau and A. Lasalmonie, Mater. Sci. Eng., 1984, Vol 67, pp. 163-182.
- [82]. H. Mecking, J. Seeger, Ch. Hartig, G. Frommeyer, 1993, ICOTOM 10.
- [83]. G. Bermig, J. Tobisch, C.Scheffzuk and C. Oertel, Mater. Sci. Forum, 1994, Vol. 157-162, pp. 309-314.
- [84]. C. Hartig, X.F. Fang, H. Mecking and M. Dahms, Acta Metall., 1992, Vol. 40, No. 8, pp. 1883-1894.

[85]. D.S. Lee, D.M. Dimiduk and S. Krishnamurthy, Mat. Res. Soc. Symp. Proc., 1993, Vol. 288, pp. 823-827.

[86]. M. Nobuki, K. Hashimoto, J. Takahashi and T. Tsujimoto, Mater. Trans. JIM., 1990, Vol. 31, pp. 814-819.

